

LIGHT CURVE SIMULATION AND SHAPE INVERSION FOR HUMAN-MADE SPACE OBJECTS

by

Liam Robinson

A Thesis

Submitted to the Faculty of Purdue University

In Partial Fulfillment of the Requirements for the degree of

Master of Science in Aeronautics and Astronautics



School of Aeronautics and Astronautics

West Lafayette, Indiana

December 2023

**THE PURDUE UNIVERSITY GRADUATE SCHOOL
STATEMENT OF COMMITTEE APPROVAL**

Dr. Carolin Frueh

School of Aeronautics and Astronautics

Dr. Kenshiro Oguri

School of Aeronautics and Astronautics

Dr. Keith LeGrand

School of Aeronautics and Astronautics

Approved by:

Dr. Gregory Blaisdell

ACKNOWLEDGMENTS

I would like to thank my advisor, Dr. Carolin Frueh, for her guidance and mentorship. Her feedback has guided me through undergraduate research, publishing a conference paper, applying for fellowships, and now writing this thesis. For that, and her continued support through my PhD, I am forever grateful.

My friends and family have also been an amazing resource throughout my research. They've helped me workshop ideas, find bugs in code, and proofread proposals. Most importantly, they've always been willing to humor my "Look at this plot I just made" requests.

Finally, I must thank my committee, Dr. Oguri and Dr. LeGrand, for their feedback and attendance at my defense. Their comments have made this thesis what it is today.

This work was supported by Katalyst grant number FA6451-22-P-0019, Boeing work number SSOW-BRT-Z0722-5045, and the National Defense Science and Engineering Graduate Fellowship through the Air Force Office of Scientific Research under grant number FA9550-18-1-0154.

TABLE OF CONTENTS

LIST OF TABLES	9
LIST OF FIGURES	10
LIST OF SYMBOLS	12
ABSTRACT	14
1 Introduction	15
1.1 State of the Art	17
2 Background	22
2.1 Time Systems	22
2.1.1 Time Scales	22
2.1.2 Julian Date	23
2.1.3 Solar and Sidereal Time	24
2.2 Coordinate Systems	25
2.2.1 Altitude References	25
Ellipsoid	25
Geoid	25
Terrain	25
2.2.2 Latitude, Longitude and Altitude	26
2.2.3 International Terrestrial Reference Frame (ITRF)	27
2.2.4 Topocentric Reference Frame (ENU)	29
2.2.5 International Celestial Reference Frame (ICRF)	29
2.2.6 Right Ascension and Declination	31
2.2.7 Azimuth and Elevation	31
2.3 Attitude	33
2.3.1 Attitude Representations	33
The Direction Cosine Matrix	33

Principal Rotation Parameters	34
Quaternions	34
2.3.2 Attitude Kinematics	35
2.3.3 Attitude Dynamics	36
2.4 Photometry	37
2.4.1 The Charge Coupled Device (CCD)	37
2.4.2 Diffraction	37
Rayleigh Criterion	37
The Airy Disk	38
2.4.3 Brightness Units	39
Irradiance	40
Apparent Magnitude	40
Normalized Irradiance	41
S_{10} Surface Brightness	42
Magnitude per Square Arcsecond	42
Candela	43
Photoelectron Counts	43
2.4.4 The Light Curve	45
3 Method	46
3.1 CCD Performance Model	46
Background Source Importance	46
3.1.1 Astronomical Spectra	48
3.1.2 Background Signal Sources	48
Airglow	48
Light Pollution	49
Twilight	50
Integrated Starlight	52
Scattered Moonlight	54
Zodiacal Light	56

Background Sampling	57
3.1.3 Sensor Effects	59
Dark Noise	59
Readout Noise	59
Truncation Noise	60
3.1.4 Signal-to-Noise Ratio (SNR)	60
3.2 Light Curve Simulation	62
3.2.1 Orbital Dynamics	62
3.2.2 Discrete Shape Representations	62
The Object File Format	62
Properties of Triangulated Meshes	63
3.2.3 Selected Satellite Models	63
3.2.4 The Bidirectional Reflectance Distribution Function	64
3.2.5 BRDF Formulations	66
Lambertian	66
Phong	66
Blinn-Phong	67
Glossy	67
Cook-Torrance	68
Oren-Nayar	68
Ashikhmin-Shirley	69
3.2.6 BRDF Summary	70
3.2.7 Simulating Light Curves for Convex Objects	70
3.2.8 Simulating Light Curves for nonconvex Objects	71
3.2.9 The Importance of Self-Shadowing	72
3.2.10 Shadow Mapping	72
3.2.11 Sampling Noisy Light Curves	74
3.3 Light Curve Shape Inversion	75
3.3.1 Direct Convex Shape Inversion	75
The Extended Gaussian Image	75

EGI Optimization	76
EGI Resampling	78
EGI Merging	79
Geometry Recovery from the EGI	80
Support Vector Optimization	82
3.3.2 Direct nonconvex Shape Inversion	82
nonconvex Feature Detection and Location	82
Concavity Creation	83
3.3.3 Shape Inversion With Noisy Measurements	85
Shape Interpolation With Signed Distance Functions	85
4 Results	88
4.1 Convex Shape Inversion Without Noise	88
4.2 nonconvex Shape Inversion Without Noise	88
4.3 Convex Shape Inversion With Noise	90
4.4 nonconvex Shape Inversion With Noise	90
5 Recommendations	91
6 Future Work	92
7 Appendices	93
7.1 Astronomical Spectra Data	93
Atmospheric Extinction	93
Quantum Efficiency	94
7.1.1 Background Source Data	95
Lunar Phase Factor	95
Scattered Moonlight	95
Zodiacal Light	96
7.1.2 Telescope Parameters	97
Purdue Optical Ground Station	97
7.1.3 File Formats	97

Wavefront OBJ Example	97
REFERENCES	99

LIST OF TABLES

2.1	WGS-84 ellipsoid model of the Earth [3]	25
3.1	Background signal importance	47
7.1	Purdue Optical Ground Station telescope parameters	97

LIST OF FIGURES

1.1	Public tracked catalog in 2000 and 2023	16
2.1	Time scales relative to TAI	23
2.2	EGM-96 geoid heights above the WGS-84 ellipsoid	26
2.3	MSL elevations surrounding the Purdue Optical Ground Station	26
2.4	ENU reference frame orientation at Purdue Optical Ground Station	29
2.5	Airy disk diffraction pattern	38
2.6	Total solar irradiance variations	40
2.7	Luminous efficiency function from [46]	44
3.1	Astronomical Spectra from [9]	48
3.2	Airmass function comparison. The Van-Rhijn factor diverges to $+\infty$ while Pickering's function reaches the correct maximum of $AM(\theta_z) \approx 40$	50
3.3	Mean airglow signal on the local observer hemisphere. The observer is in New Mexico, USA at 32.900° N, -105.533° W	51
3.4	Zenith light pollution in the eastern USA, data from [48]	52
3.5	Mean light pollution signal on the local observer hemisphere. The observer is in New Mexico, USA at 32.900° N, -105.533° W	53
3.6	Twilight model surface brightness at zenith as a function of solar zenith angle .	54
3.7	Mean twilight signal on the local observer hemisphere. The observer is in New Mexico, USA at 32.900° N, -105.533° W	55
3.8	Raw image of three GEO objects with stars streaking through the background. As expected the star signals have a variety of signal-to-noise ratios. Taken by the Purdue Optical Ground station at 32.900° N, -105.533° W by Nathan Houtz. .	56
3.9	Integrated starlight brightness map	57
3.10	Integrated starlight signal on the local observer hemisphere. The observer is in New Mexico, USA at 32.900° N, -105.533° W	58
3.11	Mean scattered moonlight signal on the local observer hemisphere. The observer is in New Mexico, USA at 32.900° N, -105.533° W	59
3.12	Mean zodiacal light signal on the local observer hemisphere. The observer is in New Mexico, USA at 32.900° N, -105.533° W	60
3.13	Selected space objects with soccer field for size reference. In order, the objects are TESS, Starlink V1, TDRS, Landsat 8, Hispasat 30W-6, Saturn V SII, TELSTAR 19V, HYLAS 4, and simplified ASTRA.	64

3.14 Implemented BRDFs rendered with arbitrary parameters, demonstrating the qualitative differences between lighting models	70
3.15 Hubble Space Telescope ray traced shadow categorization and shading. Models from [63]	72
3.16 Brightness errors introduced by neglecting shadows for Bennu and HST. Models from [63]	73
3.17 Hubble Space Telescope shadow mapping with self (red) and horizon (blue) shadows rendered. Models from [63]	73
3.18 Simplified convex, nonconvex, and open EGI nonuniqueness. Larger circles indicate greater relative areas assigned to a given normal vector.	76
3.19 Initial icosahedron EGI optimization before resampling	77
3.20 Resampled normal vectors (left) with reoptimized EGI (right)	79
3.21 Merged icosahedron EGI	80
3.22 Subdivided object (black) with reference (red) with various levels of subdivision	84
3.23 Root-adjacent and free vertices	85
3.24 SDF slice of the Stanford bunny model	86
3.25 SDF interpolation between a torus and an icosahedron	86
4.1 Collapsed house, cube, icosahedron, and box-wing satellite reconstructions using vertex displacement	88
4.2 Convex objects under vertex displacement procedure	89

LIST OF SYMBOLS

I	irradiance in $\left[\frac{W}{m^2}\right]$
\hat{I}	normalized irradiance in $[W]$
I_0	Irradiance of Vega $\left[\frac{W}{m^2}\right]$
m	Apparent magnitude [<i>nondim</i>]
JD	Julian date
T	Julian centuries
θ_{GMST}	Greenwich mean sidereal time
θ_r	Angular offset of the first zero of the Airy disk diffraction pattern
$C_{\text{Airy}}(\theta)$	CCD signal amplitude due to an Airy disk diffraction pattern [<i>ADU</i>]
k	Wavenumber
r_d	Telescope aperture radius [<i>m</i>]
d	Telescope aperture diameter [<i>m</i>]
A_{aperture}	Telescope aperture area [m^2]
f	Telescope focal length [<i>m</i>]
λ	Wavelength [<i>m</i>]
$FWHM$	Full width at half maximum
$C_{\text{Gauss}}(\theta)$	CCD signal amplitude due to a Gaussian approximation of the Airy disk [<i>ADU</i>]
$\text{STRINT}(\lambda)$	Representative zero apparent magnitude star irradiance spectrum $\left[\frac{W}{m^2 \cdot m}\right]$
$\text{QE}(\lambda)$	Quantum efficiency spectrum $\left[\frac{\text{ADU}}{m}\right]$
$\text{ATM}(\lambda)$	Atmospheric transmission spectrum $\left[\frac{1}{m}\right]$
$K_{cd}(\lambda)$	Luminous efficacy spectrum $\left[\frac{lm}{W}\right]$
SINT	CCD ADU conversion factor $\left[\frac{\text{ADU}}{W \cdot m^{-2} \cdot s}\right]$
$\text{SUN}(\lambda)$	Solar irradiance spectrum $\left[\frac{W}{m^2 \cdot m}\right]$
$\text{GLINT}(\lambda)$	Airglow radiance spectrum $\left[\frac{W}{m^2 \cdot m \cdot sr}\right]$
AINT	Intermediate airglow signal $\left[\frac{1}{s \cdot sr}\right]$
θ_z	Zenith angle [<i>rad</i>]
$\text{AM}(\theta_z)$	Relative airmass function [<i>nondim</i>]

s_{pix}	Telescope pixel scale $\left[\frac{arcsec}{pix} \right]$
Δt	CCD integration time [s]
$B_{poll,z}$	Zenith light pollution brightness in magnitudes per square arcsecond
$\bar{S}_{airglow}$	Mean airglow signal [ADU]
γ	Solar zenith angle [deg]
$B_{twi,z}$	Zenith twilight brightness in magnitudes per square arcsecond
$\bar{S}_{twilight}$	Mean twilight signal [ADU]
BINT	Zero magnitude starlight signal $\left[\frac{ADU}{s} \right]$
\bar{S}_{star}	Mean integrated starlight signal [ADU]
F_{rs}	Moonlight Rayleigh scattering radiance spectrum $\left[\frac{W}{m^2 \cdot m \cdot sr} \right]$
F_{ms}	Moonlight Mie scattering radiance spectrum $\left[\frac{W}{m^2 \cdot m \cdot sr} \right]$
F_{mt}	Total scattered moonlight radiance spectrum $\left[\frac{W}{m^2 \cdot m \cdot sr} \right]$
$f(\theta)$	Lunar brightness phase function [nondim]
\bar{S}_{moon}	Mean scattered moonlight signal [ADU]
\bar{S}_{zod}	Mean zodiacal light signal [ADU]
$\lambda_{background}$	Mean of background signal Poisson distribution [ADU]
\hat{n}	Face outward pointing unit normal vector
(v_1, v_2, v_3)	First, second, and third vertices $v_i \in \mathbb{R}^3$ on a given triangular face
h_i	Support of the ith face
\vec{E}	Extended Gaussian Image
f_r	Bidirectional Reflectance Distribution Function
L	Illumination direction unit vector
O	Observation direction unit vector
H	Halfway unit vector
C_d	Coefficient of diffuse reflection
C_s	Coefficient of specular reflection
C_a	Coeffieicnt of absorption
n	Specular exponent

ABSTRACT

Characterizing unknown space objects is an important component of robust space situational awareness. Estimating the shape of an object allows analysts to perform more accurate orbit propagation, probability of collision, and inference analysis about the object’s origin. Due to diffraction and atmospheric effects, most resident space objects of interest are unresolved when observed from the ground with electro-optical sensors. State of the art techniques for object characterization often rely on light curves — the time history of the object’s observed brightness. The brightness of the object is a function of the object’s shape, material properties, and attitude profile, along with the observation geometry. The process of recovering shape information from brightness measurements is known as the light curve shape inversion problem. This problem is ill-posed without further assumptions: modern direct shape inversion methods require that the attitude profile and material properties of the object is known, or at least can be hypothesized. This work describes improvements to light curve simulation and new methods for direct shape inversion for convex and nonconvex objects with realistic measurement noise. In particular, this work finds that improvements to the convex shape inversion process produce more accurate, sparser geometry in less time. The proposed nonconvex shape inversion method is effective at resolving singular large concave feature.

1. Introduction

Humankind has been creating space debris since the dawn of the space age [1]. Early missions like Vanguard 1, launched in March of 1958, set a precedent by leaving both their satellite and the launch vehicle's upper stage in orbit, both of which are still in orbit in 2023 [2]. Vanguard was launched into Low Earth Orbit (LEO) — defined by the European Space Agency (ESA) as any orbit with an altitude below 2000 kilometers [1]. Above LEO lies Medium Earth Orbit (MEO) for orbital altitudes between 2000 and 31570 kilometers, and Geostationary Earth Orbit (GEO) between 35586 and 35986 kilometers altitude [1]. Half a century of increasingly frequent launches has created a space environment cluttered with thousands of debris objects, increasing the number of serious conjunction events that may require avoidance maneuvers for large satellites in LEO to over 100 during 2021 [1]. While very few mission-ending collisions are occurring on a yearly basis in the early 2020s, simulations predict over 200 catastrophic collisions per year if the trend in new launches and disposal practices continue [1]. This uncontrolled proliferation of human-made space debris puts space operations at risk. High-profile satellite collisions like Iridium-Cosmos in 2009 have added fuel to the fire, producing shells of debris that further pollute LEO [3]. Anti-satellite tests carried out by the USA, Russia, China, and India since the 1960s see nations destroying their own satellites, projecting military strength at the cost of creating more debris [3]. Beyond LEO in Geostationary Transfer Orbit (GTO), exploding launch vehicle upper stages produce large amounts of debris [1]. While higher orbits are not yet as polluted as LEO, they do not decay due to atmospheric drag, allowing debris objects to remain in the environment indefinitely [3].

In the context of the modern space environment, determining the current state and predicting the future dynamics of space objects is critical for many areas of Space Domain Awareness (SDA) [4]. While the current orbits of objects can be determined accurately from astrometry — through passive optical imagery or active radar — their future dynamics are perturbed by non-conservative forces driven by their shape, attitude profile, and material properties that cannot be observed directly. In particular, objects in orbits with altitudes higher than LEO are most efficiently observed with optical telescopes as the power required

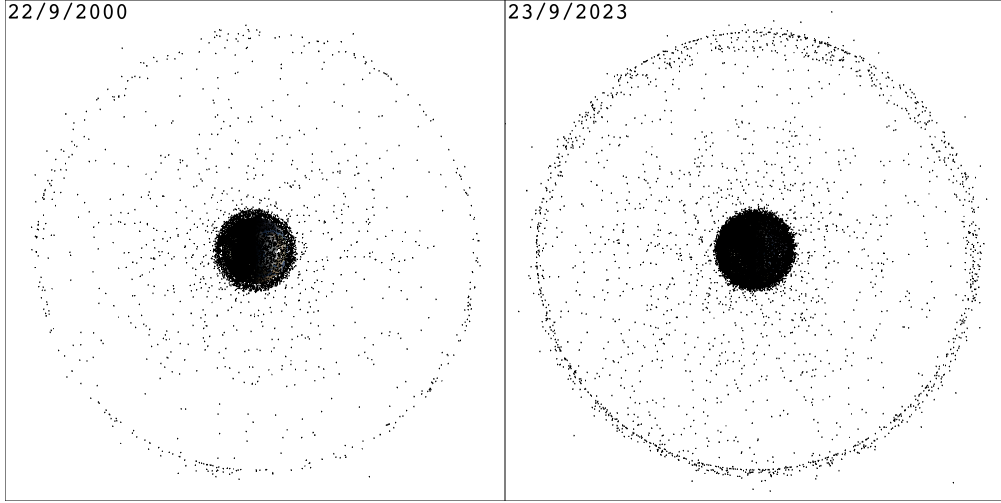


Figure 1.1. Public tracked catalog in 2000 and 2023

for radar scales with the square of the distance [4]. Because optical observations are already commonly used to characterize the orbit of the objects in orbits past LEO, it is advantageous to use the same existing sensors — or in some cases even the same images — to extract these other useful characteristics.

Characterizing an object’s shape, attitude, and material properties is fundamentally difficult as distance from the sensor and atmospheric turbulence leaves only a distribution of brightness in the image [5]. The leftover information is the total brightness of the object, and this value over time is known as the light curve. Optical brightness observations are fundamentally limited by background and sensor noise [4]. Light curves are computed from observed optical data by estimating the background mean of the image, identifying which pixels of the image likely belong to the object, subtracting the mean background level from those pixels, and calibrating the remaining object signal using known stars elsewhere in the image [6]. Each images must also be monitored for contamination from background stars and over- and under-exposures [7]. Despite these realities, the light curve is a function of the parameters of interest: the object’s shape, attitude, and material properties [5], [8]. Solving light curve shape inversion in a general case would enable robust active debris removal,

anomaly detection, and collision avoidance, all of which are benefitted by accurate shape information.

Due to the environmental noise and fundamental physical limitations on the processes driving the light curve, the measured brightness is dependent on the overall brightness and hence varies from data point to data point in the light curve. Furthermore, given the Poisson nature of the light collection process, a constant Gaussian assumption of the measurement noise in the light curve may not be suitable [5], [9]. A realistic representation of the light curve can only be achieved by accounting for the physical processes simulating the lighting and measurement process, followed by the measurement reduction and correction processing steps.

1.1 State of the Art

Light curve shape inversion was first investigated by Russell in 1906, who proposed a spherical harmonic representation that could be fit to an asteroid shape [10]. Russell noted that there would be ambiguity in the shape solution such that many solutions would fit the data equally well. The next major contribution to the field was due to Kaasalainen and Torppa in 2000, who successfully reconstructed the shapes of asteroids by directly optimizing the directions and areas of candidate faces — encapsulated by the so-called Extended Gaussian Image (EGI) — to find a convex shape that produces a similar light curve [11], [12]. Once the EGI is estimated, Kaasalainen and Torppa recover the vertices and faces of the corresponding convex object using a result of Minkowski and a nonlinear, convex optimization problem implemented by Little [13], [14]. Any EGI-based method in the asteroid or human-made object shape inversion literature uses some variation of this final stage to reconstruct the final estimated geometry. Kaasalainen and Torppa also addressed nonconvex shape inversion by optimizing a spherical harmonics shape representation to reconstruct the largest nonconvex features of an asteroid, noting that smoothness regularization was sometimes needed to prevent the shape from degenerating [11]. In the work of Kaasalainen and Torppa, the EGI optimization takes place in a single step as the asteroid shapes under study do not have sparse EGIs. By contrast, this work introduces stages that increase shape accu-

racy and lower computation time by leveraging the natural sparsity of human-made objects. Durech and Kaasalainen extended on this work in 2003 by investigating the observability of nonconvex features in asteroid light curves, finding that concave features are often observable only at high phase angles, supporting the conclusion that robust nonconvex shape inversion requires very different considerations than its convex counterpart [15]. In 2022, Chng et al. proposed a method to determine a optimal spin pole and convex shape via the EGI, offering computational benefits over Kaasalainen and Torppa while guaranteeing global optimality in the solution with respect to the input brightness data, while being limited to convex shape estimates[16]. Using the methods originally proposed by Kaasalainen and Torppa, a collaborative effort of dozens of observatories lead to the publication of Database of Asteroid Models from Inversion Techniques (DAMIT), a publicly-available repository of convex asteroid models [17]. As of October 2023, DAMIT currently hosts 16,086 models for 10,751 asteroids [18].

Shape inversion for human-made space objects differs from the asteroid inversion in a few important aspects. More diverse methods exist, being generally segmented into EGI-based methods drawing from the asteroid literature, filter-based methods for simultaneous attitude and shape solutions, and machine learning for classifying object shape from the light curve. Due to the increased number of unknowns in the material properties and attitude profile when observing an arbitrary human-made object, the inverted light curves are often simulated as part of the same work. This highlights the importance of realistic light curve simulation to effectively test proposed inversion methods.

Direct shape inversion for human-made space objects was first investigated by Calef et al., who adopted Kaasalainen and Torppa’s methods applied to multispectrum measurements to reduce the ambiguities of the different material properties common in human-made objects [19]. Bradley and Axelrad also used asteroid inversion techniques to recover convex approximations of CubeSats, rocket bodies, and box-wing satellites using the inversion codes developed and released by Kaasalainen, yielding good results for rocket body-like shapes but limited success for box-wing satellites and other high area-to-mass ratio (HAMR) objects [20]. The most recent major contributions to the direct shape inversion literature are due to Fan and Frueh, inverted the shape of convex human-made objects from noisy light curves

using the EGI with a multi-hypothesis scheme to reduce the ambiguity introduced by noisy measurements [5], [21], [22]. Fan notes that full observability is crucial for successful direct shape inversion, pointing to work by Friedman and Frueh, who quantified the observability of EGI inversion to inform sensor tasking schemes [23], [24]. Cabrera et al. applied area regularization to Fan and Friedman’s methods, achieving more accurate convex shape estimates and finding that natural constraints on the EGI area optimization renders the problem estimatable before it becomes classically observable [25]. Throughout the shape inversion literature, two themes are clear. Effective and efficient methods for nonconvex shape inversion for human-made objects are needed, and existing convex inversion methods have not been designed to work with realistic measurement noise. This work seeks to address both of these challenges by presenting a method for inverting large singular concave features in addition to a scheme for robustly inverting convex and nonconvex shapes with physically-based measurement noise.

Outside of the asteroid-inspired EGI methods, the literature falls into two broad categories: filter-based inversion, and machine learning categorization. Each offers different advantages while imposing unique limitations. Filter-based shape inversion was been pioneered by Linares through work with various co-authors. These filter-based methods often seek to perform multiple types of object characterization simultaneously, estimating attitude and material properties in addition to shape [26]–[28]. Because the input data for filter-based approaches is still only unresolved brightness measurements, estimating more properties in an already ill-posed problem requires a loss of fidelity in the solution elsewhere. Often, the shape model is highly simplified to make the problem more tractable [26]–[28]. Linares et al. have implemented unscented Kalman filters [26], multiple-model adaptive estimation algorithms [27], and adaptive Hamiltonian Markov chain Monte Carlo schemes [28] which achieve good results for simple shapes, but have not been tested on complex and realistic geometries [28]. In general, filter-based approaches are limited by the nonlinearity of highly specular and complex human-made objects, but require less information to run. Direct inversion methods that use the EGI require more *a priori* information, but are able to deliver more accurate shape estimates.

By contrast, machine learning categorization methods indirectly recover shape information by predicting which class of objects an observed light curve belongs to. Linares and Furfaro used a deep convolutional neural network to classify novel light curves as rocket bodies, payloads, or debris, achieving good classification accuracy at the cost of uncertainty about how the model would behave for light curves collected for objects outside of its training dataset [29]. Other authors, including Kerr et al. and McNally et al. have adapted the architecture developed by Furfaro et al. to classify novel light curves into an extended set of object types, demonstrating that these models are flexible enough to differentiate between many object types and attitude profiles, although with higher error rates [30], [31]. Allworth et al. applied transfer learning to classify real measurements using a synthetically-trained model, supporting the applicability of these approaches to operational decision-making [32].

There has also been significant work published on extracting light curves of human-made objects from real optical observations. Schildknecht et al. used color photometry to investigate isolate material properties of high area-to-mass ratio (HAMR) objects in GEO [6]. Karpov et al. used wide-field monitoring system to collect light curves from LEO objects [33]. Benson et al. collected light curves from retired GOES, Inmarsat, and Astra satellites in geosynchronous orbit to characterize their spin states [34]. Koshkin et al. collected light curves of TOPEX/Poseidon, among other inactive satellites, to determine their spin poles and rates [35]. Wang et al. collected light curves from GOES-8, an active GEO satellite, and simulated material properties and attitude profile to attribute peaks in its observed brightness to different parts of the spacecraft [36].

The state of the art in light curve simulation differs between approaches and the object class under study. Kaasalainen and Torppa, as well Fan, Friedman, Kobayashi, and Frueh employ a Lambertian model for convex objects with a facetwise ray tracing scheme for nonconvex objects [5], [12], [23], [37]–[39]. This approach has the advantage of being simple, but can be computationally intensive for complex objects. Allworth et al. developed a ray traced light curve simulator in based on Blender’s cycles renderer, allowing them to account for photorealistic shadowing and motion blur [32], [40]. Furfaro et al. [41] and Cabrera and Bradley [20], [25] use a simple Lambertian model with no self-shadowing. Many more authors apply a more specialized non-Lambertian Bidirectional Reflectance Distribution Function

(BRDF) for their lighting [28], [31], [42]. Throughout the literature, there is a clear gap between the simulated light curves and their observed counterparts. Due to the difference in quality, authors often treat real and simulated data very differently [32]. This work presents a physically-based lighting, shadowing, and noise model to produce synthetic light curves of similar quality to observed data, enabling more robust validation of the presented inversion techniques.

2. Background

2.1 Time Systems

2.1.1 Time Scales

There are a variety of scales used to measure time. What follows is a minimal treatment of each. For a more comprehensive overview, see Section 3.5 of [3]. International Atomic Time (TAI) is based on measurements from atomic clocks and is independent of astronomical effects or observations. By definition, TAI proceeds at the rate of 1 SI second per second. Universal Time (UT0) is derived directly from observations of the apparent position of the stars. UT1 is derived from UT0 by adjusting for polar motion. UT1 is offset from TAI by $\Delta UT1$, which is a dynamic quantity that must be continually observed. Universal Coordinated Time (UTC) is a truncation of UT1 that uses an integer number of leap seconds ΔAT to stay within 0.9 seconds of TAI. Terrestrial Time (TT) is defined by a constant offset of $TT - TAI = 32.184$ seconds from TAI and proceeding at the same rate as TAI. These time scale relations are summarized in Eq 2.1.

$$UTC = UT1 - \Delta UT1 \tag{2.1}$$

$$TAI = UTC + \Delta AT$$

$$TT = TAI + 32.184^s$$

These time scales are relevant for this research as the precise coordinate frame transformation from ITRF to the J2000.0 realization of ICRF relies on quantities expressed in UT1. Date timestamps are usually standardized to UTC, requiring the transformations in Eq 2.1 for full accuracy. Figure 2.1 shows the evolution of UTC, UT1, and TT with respect to TAI. Notice that $\Delta UT1$ continually changes while ΔAT is always truncated to a nearby integer.

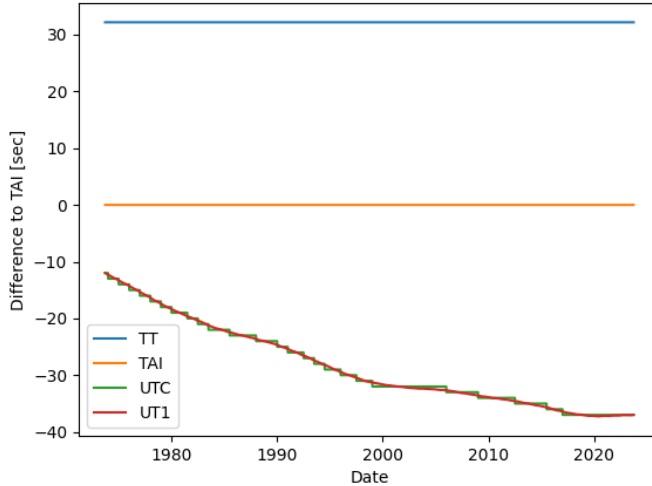


Figure 2.1. Time scales relative to TAI

2.1.2 Julian Date

Most tasks in astrodynamics are easier when using a continuous time system. For this reason, the Julian date is adopted. This quantity is defined as the number of days elapsed since January 1, 4713 B.C., at 12:00 [3]. Given a date timestamp of the form D/M/Y h:m:s between the years of 1900 and 2100, the Julian date is computed via Eq 2.2. Note that Eq 2.2 is always a function of the time scale used in the input, i.e., a UTC timestamp yields JD_{UTC} whereas a UT1 timestamp yields JD_{UT1} .

$$JD = 376Y - \text{floor} \left[\frac{7Y + 7 \cdot \text{floor} \left(\frac{M+9}{12} \right)}{4} \right] + \text{floor} \left(\frac{275M}{9} \right) + d + 1721013.5 + \frac{\frac{(s+60)}{60} + h}{24} \quad (2.2)$$

Another useful quantity for later time and coordinate system calculations is the number of Julian centuries since a particular epoch. The J2000.0 epoch is used unless otherwise stated, resulting in Eq 2.3 [3].

$$T = \frac{JD - 2451545.0}{36535} \quad (2.3)$$

Often, more specificity is needed with respect to the time scale used in Eq 2.3. For example, computing T with an input date in UT1 yields T_{UT1} using JD_{UT1} , which is in turn a function a date timestamp expressed in UT1.

2.1.3 Solar and Sidereal Time

A solar day is defined as the time required for the Sun to pass and return to an observer's meridian — a line of constant longitude extending from the geographic south pole to the geographic north pole [3]. By contrast, a sidereal day is the time required for the stars to complete a revolution around an observer's meridian. Due to the Earth's orbit around the Sun, the sidereal day is about 4 minutes shorter than the solar day [3]. The Greenwich mean sidereal time (GMST) is computed in seconds via Eq 2.4 [4].

$$\theta_{GMST} = 67310.54841 + (3.15576 \cdot 10^9 + 8640184.812866) T_{UT1} + 0.093104 T_{UT1}^2 - 6.2 \cdot 10^{-6} T_{UT1}^3 \quad (2.4)$$

Accounting for the variations in the inclination of the ecliptic ϵ and the the change in the equinox compared to the reference epoch $\Delta\Psi$ produces Greenwich apparent sidereal time (GAST) via Eq 2.5 [4].

$$\theta_{GAST} = \theta_{GMST} + \Delta\Psi \cos \epsilon \quad (2.5)$$

Both the inclination of the ecliptic and the difference in the equinox are computed with series expansions following the IAU 1980 theory of nutation [3].

2.2 Coordinate Systems

2.2.1 Altitude References

Ellipsoid

Due to Earth's equatorial bulge, it is common to model the rough shape of the Earth as an ellipsoid. In particular, the 1984 World Geodetic Survey (WGS-84) model is used throughout this work to define the shape of the Earth ellipsoid, with parameters listed in Table 2.1.

Parameter	Value
Equatorial radius R_E	6378.137 [km]
Flattening ratio f	1/298.257

Table 2.1. WGS-84 ellipsoid model of the Earth [3]

Geoid

The geoid accounts for the gravitational potential differences across the Earth's surface [3]. It is a surface of equal gravitational potential; the surface the ocean relaxes to without the influence of the wind and tides [3]. For this reason, the geoid is alternatively known as the mean sea level (MSL). The ellipsoid is a good approximation of the geoid, which deviates from the ellipsoid by less than ≈ 100 meters at all latitudes and longitudes. The height of the geoid above the ellipsoid can be computed from a high-fidelity gravity model, but it is often more convenient to interpolate a pre-computed grid of geoid heights. Figure 2.2 displays global geoid heights derived from the 1996 Earth Gravitational Model (EGM-96) relative to the ellipsoid.

Terrain

Terrain elevation is usually the final component needed to fully define the altitude of a ground station, which is often defined relative to MSL. This work uses 30-meter terrain tiles

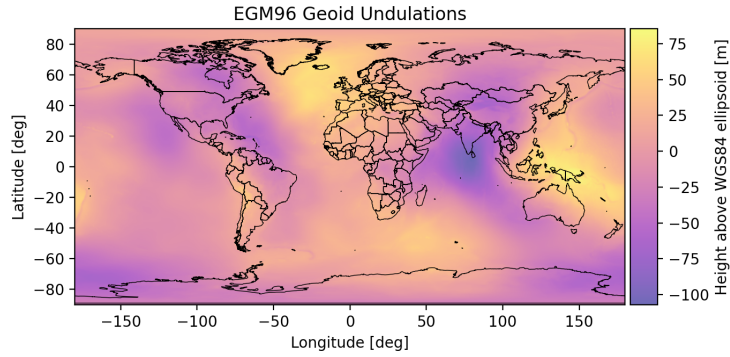


Figure 2.2. EGM-96 geoid heights above the WGS-84 ellipsoid

from the Shuttle Radar Topography Mission (SRTM). Figure 2.3 shows the local elevation around the Purdue Optical Ground Station using SRTM data.

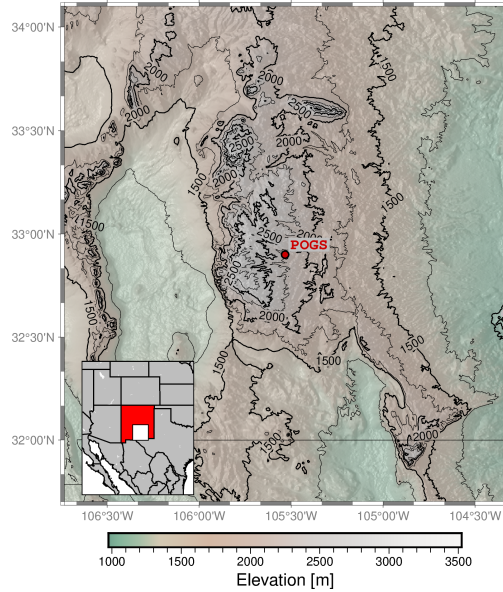


Figure 2.3. MSL elevations surrounding the Purdue Optical Ground Station

2.2.2 Latitude, Longitude and Altitude

Latitude, longitude, and altitude (LLA) are a spherical coordinates representation of position on or above the surface of the Earth. For the purposes of precise station positioning,

the difference between the two types of longitude — geocentric and geodetic — is important. Geocentric latitude is the angle between the line from the center of mass of the Earth to the position of interest and the equatorial plane. Geodetic latitude instead measures the angle between the local ellipsoid surface normal and the equatorial plane. Geodetic latitude ϕ_{geod} is converted to geocentric ϕ_{geoc} latitude with Eq 2.6 [4].

$$\phi_{\text{geoc}} = \tan^{-1} \left((1 - f)^2 \tan \phi_{\text{geod}} \right) \quad (2.6)$$

Additionally, the radius of the ellipsoid r_E at a given geocentric latitude is necessary for later conversion, expressed by Eq 2.7 [4].

$$r_E = R_E - f \sin^2(\phi_{\text{geoc}}) \quad (2.7)$$

2.2.3 International Terrestrial Reference Frame (ITRF)

The cartesian form of LLA is known as the Earth-centered Earth-fixed (ECEF) reference frame. Throughout this work, ECEF and ITRF will be used interchangeably. This frame has its origin at the center of mass of the Earth and its axes fixed in the crust. The fundamental plane of the frame is defined to be the equator — orienting the z -axis through Earth's instantaneous spin axis, and the reference direction through the intersection of the prime meridian and the equator — defining the x -axis. Completing the right-handed system with $\hat{y} = \hat{z} \times \hat{x}$ yields a reference frame that remains fixed, neglecting effects like continental drift. The transformation from LLA $(\lambda, \phi_{\text{geod}}, a)$ to ITRF is given by Eq 2.8.

$$e^2 = 2f - f^2 \quad (2.8)$$

$$N = \frac{R_E}{\sqrt{(1 - e^2 \sin(\phi_{geod})^2)}}$$

$$\rho = (N + a) \cos(\phi_{geod})$$

$$x_{itrf} = \rho \cos(\lambda)$$

$$y_{itrf} = \rho \sin(\lambda)$$

$$z_{itrf} = (N(1 - e^2) + a) \sin(\phi_{geod})$$

In Eq 2.8, e^2 is the squared eccentricity of the ellipsoid, N is the radius of curvature in the meridian, and ρ is the $x - y$ plane magnitude of the station's position [3].

Many later transformations require the body axis rotation matrices R_1 , R_2 , and R_3 which are expressed in Eq 2.9.

$$R_1(\theta) = \begin{bmatrix} 1 & 0 & 0 \\ 0 & \cos \theta & \sin \theta \\ 0 & -\sin \theta & \cos \theta \end{bmatrix} \quad (2.9)$$

$$R_2(\theta) = \begin{bmatrix} \cos \theta & 0 & -\sin \theta \\ 0 & 1 & 0 \\ \sin \theta & 0 & \cos \theta \end{bmatrix}$$

$$R_3(\theta) = \begin{bmatrix} \cos \theta & \sin \theta & 0 \\ -\sin \theta & \cos \theta & 0 \\ 0 & 0 & 1 \end{bmatrix}$$

2.2.4 Topocentric Reference Frame (ENU)

The remaining transformations in this chapter will only be defined in terms of their rotation matrices. It is often useful to express observations in a local reference frame. The East North Up (ENU) coordinate system is used throughout this work. This system has an origin at the observing station, with the first two basis vectors pointing towards the local East and North and the third pointing towards zenith. The transformation from ITRF to ENU is given by Eq 2.10.

$$\vec{r}_{enu} = F_2 F_1 R_2(\phi_{geoc}) R_3(\lambda) \vec{r}_{itr} \quad (2.10)$$

In Eq 2.10, R_3 is a rotation about the third body axis, F_1 swaps the second and third unit vectors, and F_2 swaps the first and third unit vectors. The orientation of the ENU reference frame at the Purdue Optical Ground Station is depicted in Figure 2.4.

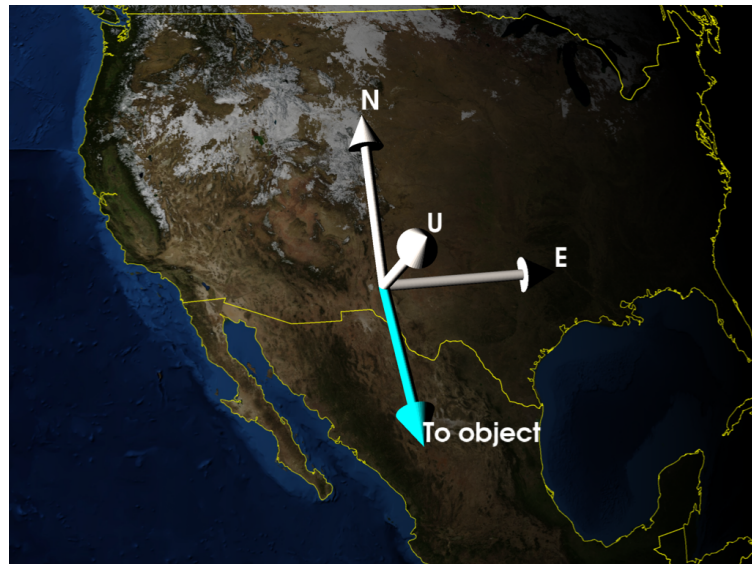


Figure 2.4. ENU reference frame orientation at Purdue Optical Ground Station

2.2.5 International Celestial Reference Frame (ICRF)

Transforming from ITRF to the a standardized inertial reference frame is an involved process due to the variety of nonlinear effects impacting the Earth's rotational motion. In

total, this transformation must account for polar motion, the nutation and precession of the Earth's pole, and the mean sidereal time. These transformations are treated much more thoroughly in Vallado [3].

Accounting for polar motion — the motion of the Earth's pole that cannot be explained through nutation theory — transforms from ITRF to Greenwich True of Date (GTOD) via Eq 2.11, where x_p and y_p are the angular components of the polar motion at the time of interest [4].

$$\vec{r}_{gtod} = R_1(y_p)R_2(x_p)\vec{r}_{itr} \quad (2.11)$$

Accounting for the sidereal rotation of the Earth about its pole transforms from GTOD to the True Equator, Mean Equinox (TEME) reference frame via Eq 2.12 [4].

$$\vec{r}_{teme} = R_3(-\theta_{GMST})\vec{r}_{gtod} \quad (2.12)$$

Accounting for the difference between GMST and GAST at the date of interest transforms from TEME to the True of Date (TOD) reference frame via Eq 2.13 [3].

$$\vec{r}_{tod} = R_3(-\Delta\Psi \cos \epsilon)\vec{r}_{teme} \quad (2.13)$$

Accounting for the nutation of Earth's pole transforms from TOD to the Mean of Date (MOD) reference frame via Eq 2.14, where $\bar{\epsilon}$ is the mean inclination of the ecliptic at the time of interest, and ϵ is the true inclination of the ecliptic [3].

$$\vec{r}_{mod} = R_1(-\bar{\epsilon})R_3(\Delta\Psi)R_1(\bar{\epsilon} + \Delta\epsilon)\vec{r}_{tod} \quad (2.14)$$

Accounting for the secular precession of Earth's pole transforms from MOD to ICRF via Eq 2.15 through the 3-2-3 Euler angle sequence (z, θ, ζ) , which are each a function of the date of the transformation [4].

$$\vec{r}_{mod} = R_3(\zeta)R_2(\theta)R_3(z)\vec{r}_{tod} \quad (2.15)$$

2.2.6 Right Ascension and Declination

Right ascension and declination, often shortened to RA/Dec, are useful angles from describing the angular position of an object on the celestial sphere from the perspective of an observer. Right ascension is defined as the angle of the observation projected onto the inertial $x - y$ plane, measured counterclockwise from inertial \hat{x} , represented by α . Declination is the angle from the $x - y$ plane to the observation with positive values above the $x - y$ plane (closer to inertial z) and negative values below. Declination is represented by δ . Given a unit vector direction $\hat{v} = [x, y, z]^T$ in inertial space, RA/Dec is computed via Eq 2.16 [4].

$$\begin{bmatrix} \alpha \\ \delta \end{bmatrix} = \begin{bmatrix} \text{atan2}(y, x) \\ \text{atan2}(z, \sqrt{x^2 + y^2}) \end{bmatrix} \quad (2.16)$$

2.2.7 Azimuth and Elevation

Azimuth and elevation, often shortened to Az/El, are similar angular quantities to right ascension and declination [4]. Instead of being based on the inertial sphere, they are referenced to an arbitrary reference frame. For a telescope making observations of an object, the local East-North-Up (ENU) frame may be used. For a satellite star tracker, star azimuth and elevation might be reported in the satellite body frame. In either case, Eq 2.16 can be repurposed in terms of Az/El, where $\hat{v} = [x, y, z]^T$ is expressed in the frame of interest [4].

$$\begin{bmatrix} Az \\ El \end{bmatrix} = \begin{bmatrix} \text{atan2}(y, x) \\ \text{atan2}(z, \sqrt{x^2 + y^2}) \end{bmatrix} \quad (2.17)$$

Note that Eq 2.17 references azimuth to the x -axis, proceeding in the counterclockwise direction. Often, this reference axis and direction may be changed depending on the reference frame being used. For example, ground station observations may be referenced to local North — the second axis of the ENU system — proceeding clockwise. This would require the substitution $Az' = \frac{\pi}{2} - Az$. Notice that this substitution leads to Az' leaking outside the domain of $[0, 2\pi)$. This is not an issue for later coordinate transformations, but

may be undesirable for plots. Wrapping the result back to the standard azimuth range via $Az_{wrapped} = \text{mod}(Az, 2\pi)$ is a sufficient fix.

2.3 Attitude

2.3.1 Attitude Representations

When discussing about the orientation of a rigid body in three dimensions, otherwise known as its attitude, that orientation is implicitly understood to be relative to some other reference frame. The direction of a unit vector can be expressed with two numbers — the azimuth and elevation of that vector. Naïvely, this could be extrapolated to conclude that six numbers are needed to express an orientation. Because the basis vectors form an orthonormal set $\{\hat{b}_1, \hat{b}_2, \hat{b}_3\}$, it follows for a right-handed system that $\hat{b}_3 = \hat{b}_1 \times \hat{b}_2$, $\hat{b}_2 = \hat{b}_3 \times \hat{b}_1$, and $\hat{b}_1 = \hat{b}_2 \times \hat{b}_3$. Each of these equations constrains one further degree of freedom, revealing that a minimum of three quantities are necessary to express the relative orientation of two reference frames. This minimum bound does not make any statements about the usefulness of three element sets; at least four dimensions are needed to remove singularities.

The Direction Cosine Matrix

The direction cosine matrix (DCM) is a 3×3 symmetric, orthogonal matrix, expressing the three basis vectors of one frame in another. This amounts to projecting each basis vector in the initial frame onto each basis vector of the final frame; the cosine of the angle between the compared vectors. It is notated with two capital letters, the rightmost indicating the reference frame of the input vectors and the leftmost indicating the transformed frame. Alternatively, the DCM is sometimes expressed as C when the frames involved are arbitrary or do not need to be denoted. For example, the DCM $[\mathcal{B}\mathcal{N}]$ takes vectors in the \mathcal{N} frame to the \mathcal{B} frame:

$${}^{\mathcal{B}}\mathbf{r} = [\mathcal{B}\mathcal{N}] {}^{\mathcal{N}}\mathbf{r} \quad (2.18)$$

The orthogonal property of the DCM implies $[\mathcal{B}\mathcal{N}]^{-1} = [\mathcal{B}\mathcal{N}]^T$ such that $[\mathcal{B}\mathcal{N}]^T = [\mathcal{N}\mathcal{B}]$.

Principal Rotation Parameters

Another common attitude representation is the Euler angle-axis set, otherwise known as principal rotation parameters [43]. Euler's rotation theorem guarantees that any relative orientation can be expressed as a single rotation about an axis $\hat{\lambda} \in \mathbb{S}^2$ by an angle $\theta \in [0, 2\pi]$ [43]. The set $\{\hat{\lambda}, \theta\}$ is known as a principal rotation parameter, abbreviated PRP hereafter. The DCM is mapped to the PRP representation via 2.19 [44].

$$\begin{aligned}\theta &= \cos^{-1} \left(\frac{1}{2} [C_{1,1} + C_{2,2} + C_{3,3} - 1] \right) \\ \hat{\lambda} &= \frac{1}{2 \sin \theta} \begin{bmatrix} C_{2,3} - C_{3,2} \\ C_{3,1} - C_{1,3} \\ C_{1,2} - C_{2,1} \end{bmatrix}\end{aligned}\quad (2.19)$$

Where $C_{i,j}$ refers to the i th row and j th column of C . The mapping from PRP to DCM is also relatively straightforward.

$$C = I_3 + \sin \theta [\hat{\lambda} \times] + (1 - \cos \theta) [\hat{\lambda} \times]^2 \quad (2.20)$$

Where $[\mathbf{v} \times]$ is the matrix cross product operator, defined on $\mathbf{v} \in \mathbb{R}^3$ as:

$$[\mathbf{v} \times] = \begin{bmatrix} 0 & -v_3 & v_2 \\ v_3 & 0 & -v_1 \\ -v_2 & v_1 & 0 \end{bmatrix}. \quad (2.21)$$

This operator is useful as it rephrases the cross product as matrix multiplication, i.e. $\mathbf{v} \times \mathbf{u} = [\mathbf{v} \times] \mathbf{u}$. While the PRP $\{\theta, \hat{\lambda}\}$ is a four element set, there are only three degrees of freedom due to the unit norm constraint on $\hat{\lambda}$.

Quaternions

The quaternion represents attitude with a point on the surface of the hypersphere \mathbb{S}^3 . In terms of the PRP, the quaternion is given by Eq 2.22 [43].

$$\mathbf{q} = \begin{bmatrix} \hat{\lambda} \sin(\theta) \\ \cos(\theta) \end{bmatrix} \quad (2.22)$$

The first three entries of the quaternion are often called the vector component, with the final entry being the scalar component. Some authors reorder the quaternion, placing the scalar term first. Often the entries of a single quaternion are referenced by index such that $\mathbf{q} = [q_1, q_2, q_3, q_4]$. Similarly, the vector portion of the quaternion is referenced with $\mathbf{q}_{1:3}$. The quaternion can be mapped back to the PRP [43] via

$$\begin{aligned} \theta &= \cos^{-1}(q_4) \\ \lambda &= \frac{\mathbf{q}_{1:3}}{\sin \theta}. \end{aligned} \quad (2.23)$$

The quaternion maps to the DCM [43] via

$$C = \begin{bmatrix} -q_2^2 - q_3^2 + q_1^2 + q_4^2 & 2q_1q_2 + 2q_3q_4 & 2q_1q_3 - 2q_2q_4 \\ 2q_1q_2 - 2q_3q_4 & -q_1^2 - q_3^2 + q_2^2 + q_4^2 & 2q_1q_4 + 2q_2q_3 \\ 2q_1q_3 + 2q_2q_4 & 2q_2q_3 - 2q_1q_4 & -q_1^2 - q_2^2 + q_3^2 + q_4^2 \end{bmatrix} = \Xi(q)^T \Psi(q). \quad (2.24)$$

In Eq 2.24, Ψ is defined to be [43]

$$\Psi = \begin{bmatrix} q_4 & q_3 & -q_2 \\ -q_3 & q_4 & q_1 \\ q_2 & -q_1 & q_4 \\ -q_1 & -q_2 & -q_3 \end{bmatrix}. \quad (2.25)$$

2.3.2 Attitude Kinematics

Because it is cheap to convert between attitude representations, only one set of kinematic equations are needed for propagating a rigid body attitude profile from an initial con-

dition. Quaternion kinematic differential equations are chosen as they have no singularity and produce very smooth dynamics that are easy to integrate when compared to three-variable representations that possess singularities. Given the current orientation quaternion $\mathbf{q} = [q_1, q_2, q_3, q_4]^T$ and angular velocity $\omega = [\omega_1, \omega_2, \omega_3]^T$ the quaternion derivative is computed via Eq 2.26

$$\begin{bmatrix} \dot{\epsilon}_1 \\ \dot{\epsilon}_2 \\ \dot{\epsilon}_3 \\ \dot{\epsilon}_4 \end{bmatrix} = \frac{1}{2} \begin{bmatrix} \epsilon_4 & -\epsilon_3 & \epsilon_2 & \epsilon_1 \\ \epsilon_3 & \epsilon_4 & -\epsilon_1 & \epsilon_2 \\ -\epsilon_2 & \epsilon_1 & \epsilon_4 & \epsilon_3 \\ -\epsilon_1 & -\epsilon_2 & -\epsilon_3 & \epsilon_4 \end{bmatrix} \begin{bmatrix} \omega_1 \\ \omega_2 \\ \omega_3 \\ 0 \end{bmatrix}. \quad (2.26)$$

2.3.3 Attitude Dynamics

Rigid body dynamics can be easily expressed in the body principal axes with an arbitrary torque $\mathbf{M} = [M_1, M_2, M_3]^T$ in the same frame via Eq 2.27

$$\begin{bmatrix} \dot{\omega}_1 \\ \dot{\omega}_2 \\ \dot{\omega}_3 \end{bmatrix} = \begin{bmatrix} (M_1 + I_2\omega_2\omega_3 - I_3\omega_2\omega_3) / I_1 \\ (M_2 - I_1\omega_1\omega_3 + I_3\omega_1\omega_3) / I_2 \\ (M_3 + I_1\omega_1\omega_2 - I_2\omega_1\omega_2) / I_3 \end{bmatrix}. \quad (2.27)$$

Equations 2.27 and 2.26 are numerically integrated to yield the orientation time history which is necessary for later light curve simulations.

2.4 Photometry

2.4.1 The Charge Coupled Device (CCD)

Many optical telescopes, including the Purdue Optical Ground Station, use a CCD to convert incident photons into a digital signal on a pixel grid [9]. CCDs accomplish this with a matrix of semiconductor pixel wells which collect electrons released by the photoelectric effect when photons are incident on that pixel [9]. The release of these photoelectrons is wavelength dependent and is captured by the quantum efficiency spectrum of a given CCD. Developing this background in photometry is useful for both light curve simulation as well as simulating the CCD camera measuring that light curve.

2.4.2 Diffraction

Rayleigh Criterion

Many objects of interest are far past low-Earth orbit, making optical observations diffraction limited. Diffraction is always occurring when observing an object at any distance through any optics, but it begins to dominate when the object's scale is equal or smaller than the Rayleigh criterion. The Rayleigh criterion states that light of wavelength λ will spread into a diffraction pattern with the first minimum of the distribution at an angular radius θ_R when passing through a circular aperture of diameter d such that:

$$\sin \theta_R = 1.22 \frac{\lambda}{d}. \quad (2.28)$$

For a 1-meter aperture optical telescope observing a 10-meter diameter object in GEO — giving an angular radius of $\approx 10^{-7}$ radians — Eq 2.28 predicts that the diffraction pattern will be 5 times wider than the object. As a result, GEO objects cannot be resolved from the ground, independent of atmospheric effects.

The Airy Disk

The far-field diffraction pattern produced by a point source is known as an Airy pattern [4]. The Airy disk is expressed in terms of an amplitude C at an angular distance θ from the center $C(\theta)$ as:

$$C_{\text{Airy}}(\theta) = C_0 \left(\frac{2J_1(k \cdot r_d \sin \theta)}{k \cdot r_d \sin \theta} \right). \quad (2.29)$$

In Eq 2.29, C_0 is the amplitude of the center of the Airy disk, r_d is the radius of the aperture, $k = \frac{2\pi}{\lambda}$ is the wavenumber, and J_1 is the first order Bessel function of the first kind. The central magnitude C_0 is expressed:

$$C_0 = \frac{S_{\text{obj}}^2 A_{\text{aperture}}^2}{2f^4}. \quad (2.30)$$

In Eq 2.30, S_{obj} is the total mean irradiance incident on the CCD due to the source, A_{aperture} is the aperture area, and f is the focal length of the optics [4]. The pattern produced by Eq 2.29 is depicted in Figure 2.5.

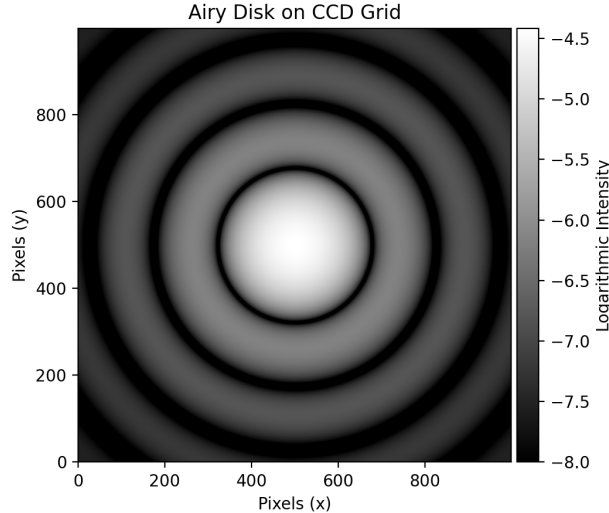


Figure 2.5. Airy disk diffraction pattern

The Rayleigh criterion expresses the angular size of the first zero of the Airy disk, after which the amplitude of the Airy disk drops off exponentially. It is often useful to approximate

the Airy disk with a 2D Gaussian. We can fit this Gaussian with a single parameter — the full width at half maximum (FWHM). The FWHM expresses the diameter at which the signal drops to half the magnitude of its central maximum [4]. The FWHM of the Airy disk is expressed:

$$FWHM_{\text{airy}} = \frac{1.028\lambda}{2r_d}. \quad (2.31)$$

The diffraction pattern is not the only effect that spreads the unresolved signal over the pixel grid. Atmospheric turbulence contributes to further spreading and speckling of the signal [4]. This effect — known as the *seeing* — is encapsulated in $FWHM_{\text{seeing}}$ and is generally between 1 and 3 arcseconds [4]. While the seeing and diffraction pattern are additive, it is sufficient to take the larger value for simulation purposes [4]. The standard deviation of the Gaussian approximation of the Airy disk is given by:

$$\sigma = \frac{FWHM}{2\sqrt{2 \ln 2}}. \quad (2.32)$$

The full Gaussian approximation at an angular distance θ from the source is given by:

$$C_{\text{Gauss}}(\theta) = \frac{0.838\bar{C}_{\text{all}}}{2\pi\sigma^2} \exp\left(-\frac{\theta^2}{2\sigma^2}\right) \quad (2.33)$$

In practice, computing the Airy disk or its Gaussian approximation on rectangular pixel grid amounts to integrating the amplitude function $C(\theta)$ over the pixel area:

$$C_{\text{pix}}(x, y) = \int_x^{x+\Delta x} \int_y^{y+\Delta y} C(\theta(x, y)) dy dx. \quad (2.34)$$

2.4.3 Brightness Units

In the context of photometry, "brightness" is a catch-all term for a variety of units. Let's explore the relationships between these units to make later conversions more clear.

Irradiance

Irradiance is the standard SI linear unit used to describe the total amount of energy incident on a surface from a given source. An irradiance of $1 \left[\frac{W}{m^2} \right]$ implies that a $10 [m^2]$ area would experience $10 [W]$ of incident power. The mean irradiance of the Sun — termed the solar constant — is derived from the mean luminosity of the Sun $L_s = 3.828 \cdot 10^{26} [W]$ and a distance of 1 Astronomical Unit $1 [AU] = 149597870.7 [km]$ [4]. The mean solar constant is then computed via

$$I_0 = \frac{L_s}{4\pi(AU)^2} \approx 1361.0 \left[\frac{W}{m^2} \right]. \quad (2.35)$$

In reality, the exoatmospheric irradiance at Earth varies [4]. Figure 2.6 displays the small variations in the solar irradiance due to the solar cycle and the much larger variations due to Earth's eccentric orbit.

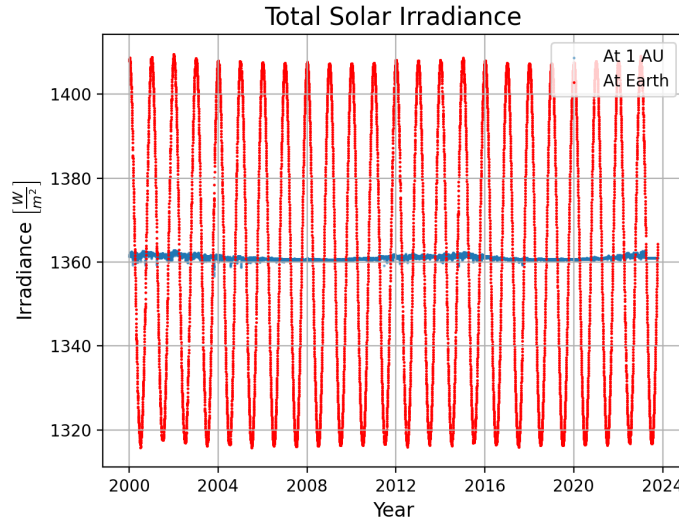


Figure 2.6. Total solar irradiance variations

Apparent Magnitude

Apparent magnitude — also known as visual or relative magnitude — is a reverse logarithmic scale that originates in astronomy [4]. Stellar sources span many orders of magnitude

of brightness, making a logarithmic scale a helpful middle ground for comparison. Note that apparent magnitude always expresses brightness at the observer's location; absolute magnitude is a different quantity that normalizes brightness from a distance of 10 parsecs [4]. Apparent magnitude m is computed from irradiance via Eq 2.36.

$$m = -2.5 \log_{10} \left(\frac{I}{I_0} \right) \quad (2.36)$$

In Eq 2.36, I is the irradiance of the source of interest and I_0 is irradiance of the zero-point source. This makes sense; substituting $I = I_0$ returns $m = 0$. The star Vega is usually taken to be the zero-point with irradiance $I_0 = 2.518021002 \cdot 10^{-8} \left[\frac{W}{m^2} \right]$ [4].

We can rearrange Eq 2.36 to compute irradiance from a given apparent magnitude, yielding Eq 2.37.

$$I = I_0 \cdot 10^{-\frac{m}{2.5}} \quad (2.37)$$

Normalized Irradiance

The light curve simulation methods presented in this work heavily use normalized irradiance, the irradiance of a source observed from a distance of 1 meter. This is a non-standard quantity in the literature, but proves useful for the same reasons absolute magnitude is used by astronomers. Adjusting sources to be at a standard distance allows us to simulate and invert light curves in a non-dimensionalized space. This simplifies simulation and makes the shape inversion optimizations more robust. To make the conversion explicit, irradiance observed at a distance r in meters from an object is converted to normalized irradiance \hat{I} in watts via Eq 2.38.

$$\hat{I} = r^2 I \quad (2.38)$$

S₁₀ Surface Brightness

While apparent magnitude and irradiance are effective for quantifying the flux of point sources, other units exist to describe diffuse or extended sources where brightness is spread over an area. S_{10} is a unit of surface brightness representing the number of 10th magnitude stars per square degree that would produce the same flux as a given diffuse source. Surface brightness in S_{10} over a given solid angle Ω [sr] can be converted to total irradiance I [$\frac{W}{m^2}$] via Eq 2.39.

$$\frac{I \left[\frac{W}{m^2} \right]}{S_{10}} = 10^{-10/2.5} \left(\Omega \frac{180^2}{\pi^2} \right) \int_{10^{-8}}^{10^{-6}} \text{STRINT}(\lambda) d\lambda = 8.26617 \Omega \cdot 10^{-9} \quad (2.39)$$

In 2.39, $\text{STRINT}(\lambda) \left[\frac{W}{m^2 \cdot m} \right]$ is the representative spectrum of a 0th magnitude star, $\text{QE}(\lambda)$ is the quantum efficiency spectrum of the observing sensor, $\text{ATM}(\lambda)$ is the atmospheric transmission spectrum, $\lambda [m]$ is wavelength, $h \left[\frac{m^2 \cdot kg}{s} \right]$ is Plank's constant, and $c \left[\frac{m}{s^2} \right]$ is the speed of light in vacuum. Quantum efficiency has units of photoelectrons which conveys the fraction of incident photons which are (proportionally) converted to photoelectrons in the CCD sensor. Atmospheric transmission is a unitless quantity conveying the fraction of light that is not absorbed by the atmosphere. Example spectra for $\text{ATM}(\lambda)$ and $\text{QE}(\lambda)$ are displayed in Figure 3.1, with underlying data provided in Appendices 7.1 and 7.1.

Magnitude per Square Arcsecond

A second surface brightness unit is $\left[\frac{\text{mag}}{\text{arcsec}^2} \right]$, also known as MPSAS (magnitude per square arcsecond). This quantity can be thought of as a generalized S_{10} , where instead of quantifying the number of stars of a certain magnitude in a solid angle, the equivalent magnitude of a single point source is measured. A surface brightness B_{10} in S_{10} can be converted into surface brightness B_{mag} in $\left[\frac{\text{mag}}{\text{arcsec}^2} \right]$ via Eq 2.40.

$$B_{\text{mag}} = -2.5 \log_{10} \left(\frac{B_{10} \cdot 10^{-4}}{12960000} \right) \quad (2.40)$$

In Eq 2.40 S_{10} is first converted to the total irradiance per square degree, convert square degrees to square arcseconds, and transform the result back into apparent magnitude. MPSAS is converted to irradiance per steradian via Eq 2.41 using 2.37.

$$I = \left(\frac{180}{3600\pi} \right)^2 I_0 \cdot 10^{-\frac{MPSAS}{2.5}} \quad (2.41)$$

Candela

Some light pollution datasets are given in units that include candela. Candela is the SI base unit of luminous intensity defined by the International Committee for Weights and Measures as "Fixing the numerical value of the luminous efficacy of monochromatic radiation of frequency $540 \cdot 10^{12}$ Hz to be equal to exactly 683" [45]. This means that an isotropic green light source with frequency $540 \cdot 10^{12}$ Hz ($\lambda = 555$ nm) has a luminous efficacy of $K_{cd} = 683$ [lm/W] where lm stands for lumens. Luminous efficacy itself determines how well a source produces visible light. For a given wavelength, candela B_{cd} is converted to watts per steradian B_{wsr} via Eq 2.42 [45]

$$B_{wsr}(\lambda) = \frac{B_{cd}}{K_{cd}(\lambda)}. \quad (2.42)$$

The luminous efficiency function $K_{cd}(\lambda)$ models the human eye's response to the visible spectrum [46]. Different fits of this function exist; the function proposed Sharpe et al. is adopted, displayed in Figure 2.7 [46].

Candela per unit area can be converted into MPSAS by combining Eq 2.42 with 2.36, yielding Eq 2.43, which is still a function of the source's wavelength.

$$MPSAS(\lambda) = -2.5 \log_{10} \left(\frac{B_{cd}}{\left(\frac{180}{3600\pi} \right)^2 K_{cd}(\lambda) I_0} \right) \quad (2.43)$$

Photoelectron Counts

Accurately simulating measured light curves requires an accurate simulation of the CCD camera taking the image. The first step towards that is understanding how irradiance at

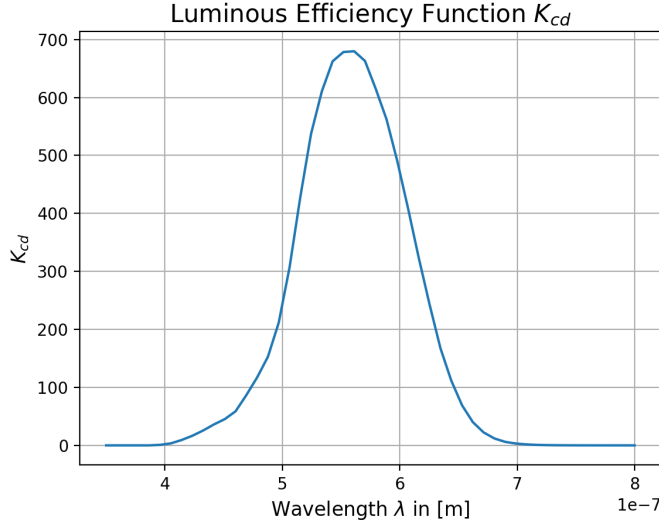


Figure 2.7. Luminous efficiency function from [46]

the telescope aperture is converted into pixel values in the final image. Raw images taken by a CCD-equipped telescope have pixel values measured in photoelectron counts, otherwise known as Analog-to-Digital Units (ADU) [9]. The count in a single pixel obtained is directly proportional (via the CCD's gain) to the number of photons incident on that pixel during the integration time. Higher order effects in the silicon of the CCD makes this description incomplete, but for non-resolved imaging applications concerned about, effects smaller than the sensor readout noise and dark current can be safely neglected [4]. Irradiance can be converted to ADU via the conversion factor $SINT$ in Eq 2.44 [9].

$$SINT = A_{aperture} \int_{10^{-8}}^{10^{-6}} \left(\frac{SUN(\lambda)}{I_{sun}} \right) \cdot QE(\lambda) \cdot ATM(\lambda) \cdot \left(\frac{\lambda}{hc} \right) d\lambda \quad (2.44)$$

In Eq 2.44, $SUN(\lambda)$ is the spectrum of solar irradiance in $\left[\frac{W}{m^2 \cdot m} \right]$, I_{sun} is the irradiance of the Sun (generally taken to be the solar constant 1361 $\left[\frac{W}{m^2} \right]$). Read literally, the integral term as units $\left[\frac{1}{Ws} \right]$, giving the number of counts per incident Watt of solar radiation and second of integration time. The aperture diameter factor outside the imintegral accounts for the area of light incident on the CCD, giving SINT units of $\left[\frac{m^2}{Ws} \right]$. The spectra in Eq 2.44 are plotted in Figure 3.1 with data in Appendix 7.1. Multiplying by irradiance in $\left[\frac{W}{m^2} \right]$ and

an integration time Δt in seconds will yield the mean photoelectron signal \bar{C}_{all} in ADU as shown in Eq 2.45.

$$\bar{C}_{all} = \text{SINT} \cdot I \cdot \Delta t \quad (2.45)$$

For completeness, irradiance can be recovered from a signal in ADU and the integration time via Eq 2.46.

$$I = \frac{S}{\text{SINT} \cdot \Delta t} \quad (2.46)$$

2.4.4 The Light Curve

TODO: this

3. Method

3.1 CCD Performance Model

Whenever an optical telescope is observing an unresolved space object, the object’s signal is necessarily superimposed on whatever signals exist in the background as the unresolved signal spreads much further than the object’s actual geometric bounds. In this context, background does not only refer to sources physically further than the object — as light can easily enter optical path through atmospheric scattering — but all sources that impact the image apart from the object signal. Some of these sources even originate within the telescope optics and its sensor. To faithfully simulate a telescope observing an object, many position-based SDA tasks are able to ignore background effects while acquiring or tracking objects. For photometry-based SDA, the background is critical. The overall noise floor can be broken up into background signal sources and sensor effects.

Background Source Importance

Some background signals are more impactful than others. For simulating realistic light curves, it is important to only model those background sources that have the possibility of being at or above the order of magnitude of the object signal, thereby seriously degrading the signal to noise ratio. As a baseline, the background terms modeled by Krag for the PROOF CCD performance model were implemented, namely scattered moonlight, airglow, zodiacal light, and integrated starlight [9]. In addition, twilight and light pollution models were implemented to increase the time and station location flexibility of the simulation. Each background term is modeled at medium fidelity — often using tabulated measurements or set of exponential distributions to govern the scattering physics. As a result, this background performance model does not capture local weather conditions or precisely simulate the scattering of each photon through the atmosphere, but still strives to faithfully models the physics of each background signal process. Table 3.1 ranks the approximate magnitudes in photoelectrons per pixel one can expect from a telescope similar to the Purdue Optical Ground Station.

Source	Magnitude [e⁻/pix]
Twilight	$10^1 - 10^7$
Scattered moonlight	$0 - 10^5$
Airglow	$10^3 - 10^4$
Zodiacal light	$10^2 - 10^4$
Light pollution	$10^2 - 10^3$
Integrated starlight	$10^1 - 10^2$

Table 3.1. Background signal importance

3.1.1 Astronomical Spectra

Four of the quantities needed for the background model vary with wavelength. These are the atmospheric transmission, the sensor quantum efficiency, the irradiance of a 0th magnitude star, and the solar spectrum. Each spectrum is displayed in Figure 3.1.

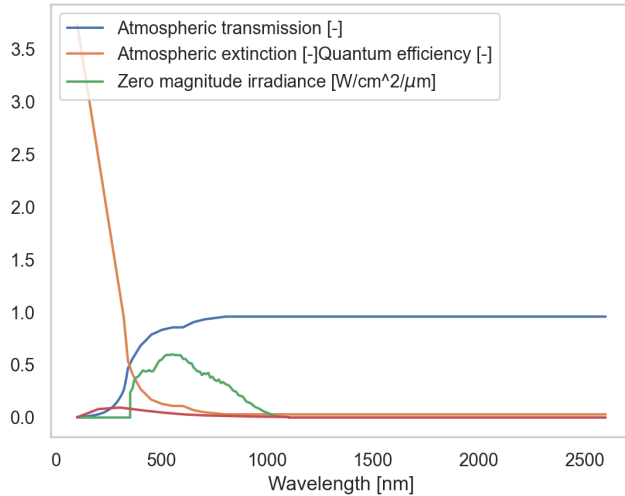


Figure 3.1. Astronomical Spectra from [9]

In practice, the quantum efficiency curve varies by sensor and the thermal conditions of the observation. The curve adopted in this work is that used by Krag; modern sensors will often perform better.

3.1.2 Background Signal Sources

Airglow

Certain chemical reactions from 80-110 km altitude in the upper atmosphere release visible light [9]. This effect is known as airglow. Since these reactions are assumed to be isotropic — equally intense when integrated along any vertical line extending upwards from the surface. The airglow signal AINT is modeled in a similar fashion to integrated starlight. Given the airglow spectra $\text{GLINT}(\lambda)$ $\left[\frac{W}{m^2 \cdot m \cdot sr}\right]$, the airglow signal is computed via Eq 3.1 [9].

$$\text{AINT} = A_{\text{aperture}} \int_{10^{-8}}^{10^{-6}} \text{GLINT}(\lambda) \cdot \text{QE}(\lambda) \cdot \text{ATM}(\lambda) \cdot \left(\frac{\lambda}{hc} \right) d\lambda \quad (3.1)$$

The quantity AINT has units $\left[\frac{1}{\text{s}\cdot\text{sr}} \right]$, meaning that the mean airglow signal in ADU per pixel is simply given by Eq 3.2

$$\bar{S}_{\text{airglow}} = \text{AINT} \cdot \text{AM}(\theta_z) \cdot \Delta t \cdot \left(\frac{\pi s_{\text{pix}}}{648000} \right)^2 \quad (3.2)$$

In Eq 3.2, $\text{AM}(\theta_z)$ is the relative airmass function which accounts for the accumulation of air along the optical path at different zenith angles [4]. This airmass is termed *relative* as it relates the ratio of absolute airmass at a zenith angle to the absolute airmass at zenith. Often, this function is approximated by the Van-Rhijn factor $\text{AM}(\theta_z) = \sec \theta_z$ which remains accurate up to $\theta_z \approx 70^\circ$ before diverging to infinity. Instead, a function proposed by Pickering is used [47].

$$\text{AM}(\theta_z) = \frac{1}{\sin \left((90 - \theta_z) + \frac{244}{165 + 47 * (90 - \theta_z)^{1.1}} \right)} \quad (3.3)$$

Using Eq 3.3 instead of the Van-Rhijn factor is important for computing background signals near the horizon. Figure 3.2 displays this comparison in action.

Light Pollution

Another source of background noise light pollution. On a cloudless night with low levels of atmospheric aerosols, the zenith surface brightness is approximately $22 \left[\frac{\text{mag}}{\text{arcsec}^2} \right]$ (MPSAS) [9]. As light pollution increases, this zenith brightness may dip down to $14 - 15 \left[\frac{\text{mag}}{\text{arcsec}^2} \right]$. To get accurate localized zenith brightness values, we use the 2015 World Atlas of Sky Brightness dataset [48]. The data is reported in $\left[\frac{\text{mcd}}{\text{cm}^2} \right]$ on a 30-arcsecond grid, requiring conversion to a more useful unit. A subset of the global dataset is displayed in 3.4 This conversion is listed in Eq 2.43, using a monochromatic $\lambda = 474 \text{ nm}$ to fit Falchi et al.'s example conversions [49].

The mean light pollution CCD signal in ADU per pixel is formulated similarly to airglow. The station's zenith surface brightness $B_{\text{poll},z}$ in MPSAS, linearly interpolated from the World

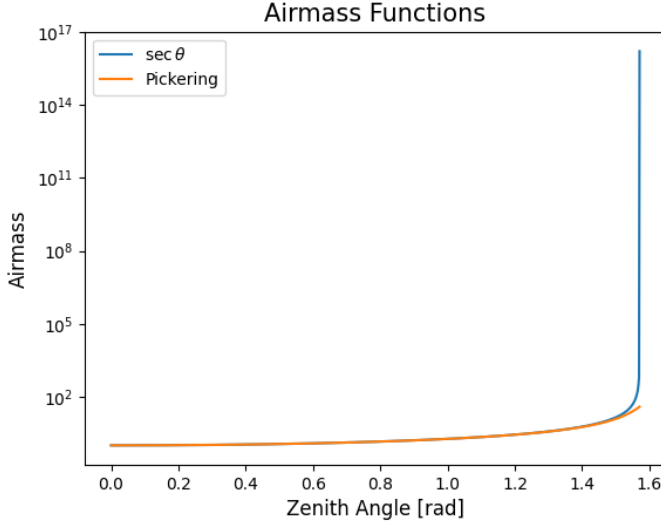


Figure 3.2. Airmass function comparison. The Van-Rhijn factor diverges to $+\infty$ while Pickering’s function reaches the correct maximum of $\text{AM}(\theta_z) \approx 40$.

Atlas dataset, is converted to irradiance per steradian via 2.41 and to ADU per pixel via 3.4. Note that Krag does not implement a specific light pollution model, but instead takes the dark sky site zenith brightness of 22 MPSAS as input to an atmospherically scattered light model. This is simply an adaptation of Krag’s model with a variable zenith brightness.

$$\bar{S}_{pollution} = B_{poll,z} \cdot SINT \cdot \text{AM}(\theta_z) \cdot \Delta t \cdot \left(\frac{\pi s_{pix}}{648000} \right)^2 \quad (3.4)$$

Twilight

Even after the Sun sets, scattered sunlight in the upper atmosphere creates a signal on our CCD. The twilight model implemented for this work is due to Patat et al. and was developed for the European Southern Observatory at Paranal in Chile [50]. This model implements the zenith brightness as a function of the solar zenith angle γ — the angle from zenith to the Sun’s apparent centroid. Patat et al.’s model fits a second-degree polynomial in γ to approximately 2000 observations in varying atmospheric conditions, yielding separate

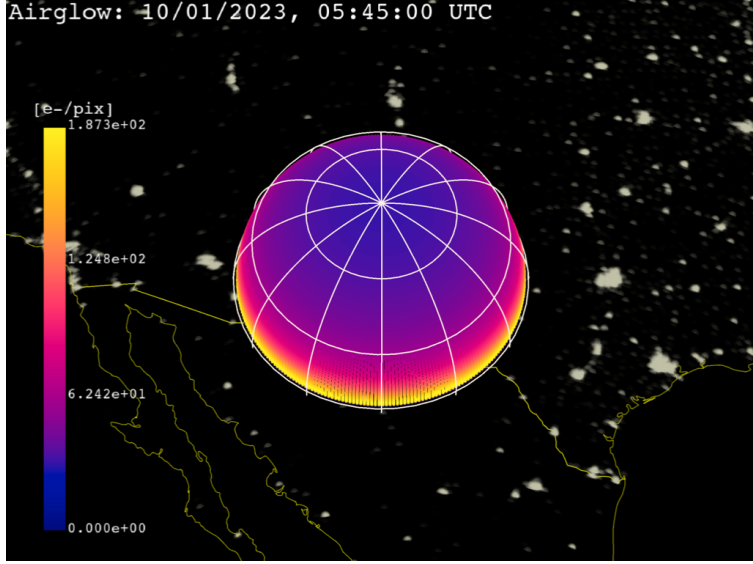


Figure 3.3. Mean airglow signal on the local observer hemisphere. The observer is in New Mexico, USA at 32.900° N, -105.533° W

curves for each of the UBVRI passbands. For example, for the V band, the twilight zenith brightness in MPSAS is given by 3.5 [50].

$$B_{twi,z} = 11.84 + 1.518(\gamma - 95^{\circ}) - 0.057(\gamma - 95^{\circ})^2 \quad (3.5)$$

Eq 3.5 is valid from $95^{\circ} \leq \gamma \leq 105^{\circ}$. While $\gamma \leq 95^{\circ}$, the zenith brightness is taken to be constant and equal to the brightness at $\gamma = 95^{\circ}$. This is not accurate, as it predicts daylight to be the brightness of twilight, but is sufficiently bright to correctly forbid daytime observations by lowering the SNR drastically. After $\gamma = 105^{\circ}$ the zenith surface brightness is set to $B_{twi,z} = 22$ MPSAS to match the optimal observation condition of the light pollution model [9]. Zenith twilight brightness is plotted as a function of γ in Figure 3.6.

Computing the mean CCD signal in ADU per pixel due to the twilight brightness proceeds identically to the light pollution formulation.

$$\bar{S}_{twilight} = B_{twi,z} \cdot SINT \cdot AM(\theta_z) \cdot \Delta t \cdot \left(\frac{\pi s_{pix}}{648000} \right)^2 \quad (3.6)$$

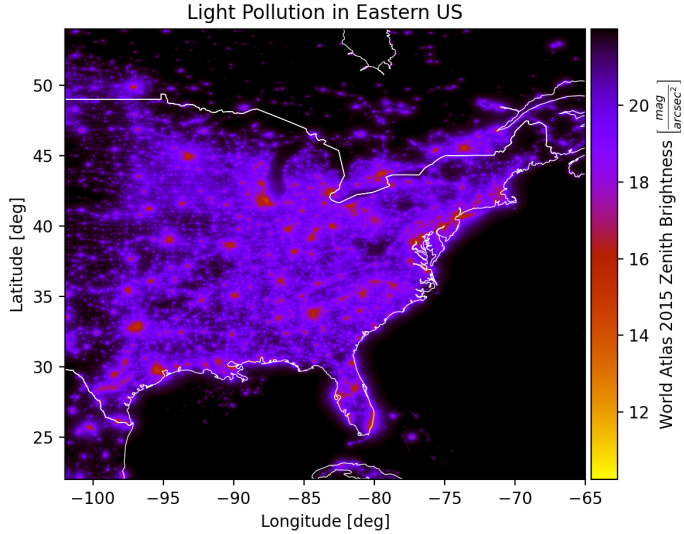


Figure 3.4. Zenith light pollution in the eastern USA, data from [48]

Integrated Starlight

Stars are almost always present in optical images of space objects. The brightest stars streaking across the field of view in Figure 3.8 have high SNRs and stand out clearly against the dark background. This raises a question: if the telescope observes a full $1^\circ \times 1^\circ$ area of the sky, where are the rest of the stars? The Milky Way alone contains approximately $1 \cdot 10^{11}$ stars. The answer is clear: many more stars are present in the image, most of them falling into the background. This residual faint starlight is called "integrated" starlight.

Krag [9] modeled this signal by building a $1^\circ \times 1^\circ$ grid of surface brightness values for the full inertial sphere, parameterized by RA/Dec. Krag used the Guide Star catalog, which contains 15 million stars down to apparent magnitude 16. Exponential extrapolation was used to predict star counts in each bin for higher magnitudes [9]. Twenty years later, larger star catalogs exist that are nearly complete to much higher apparent magnitudes. The integrated starlight catalog used in this work was built from the GAIA catalog with approximately 1.5 billion stars down to magnitude 21-22 [51]. The same $1^\circ \times 1^\circ$ grid was computed using GAIA [52], resulting in Figure 3.9 which shows the computed brightness map in units of S_{10} .

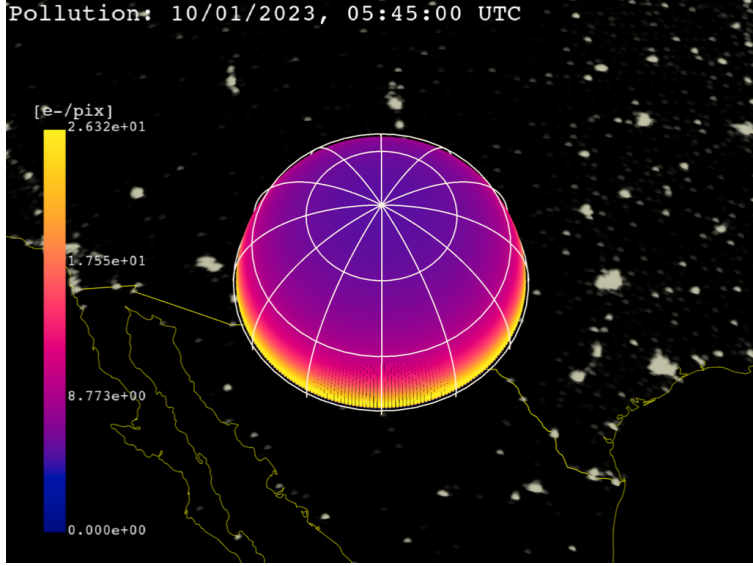


Figure 3.5. Mean light pollution signal on the local observer hemisphere. The observer is in New Mexico, USA at 32.900° N , -105.533° W

With this map of exoatmospheric mean brightness of the night sky due to integrated starlight, the corresponding signal mean in the telescope CCD is computed, adopting Krag's formulation [9].

$$\text{BINT} = A_{\text{aperture}} \int_{10^{-8}}^{10^{-6}} \text{STRINT}(\lambda) \cdot \text{QE}(\lambda) \cdot \text{ATM}(\lambda) \cdot \left(\frac{\lambda}{hc} \right) d\lambda \quad (3.7)$$

In Eq 3.7, D is the telescope aperture diameter in meters, h is Plank's constant in $\left[\frac{m^2 kg}{s} \right]$, and c is the speed of light in vacuum in $\left[\frac{m}{s} \right]$. The resulting quantity BINT has units of $\left[\frac{1}{s} \right]$, representing the mean total photons passing through the telescope aperture due to integrated starlight.

$$\bar{S}_{\text{star}} = 10^{-4} \cdot \text{BINT} \cdot \left(\frac{s_{\text{pix}}}{3600} \right)^2 \cdot \Delta t \cdot b_{\text{is}} \quad (3.8)$$

In Eq 3.8, b_{is} is the integrated starlight brightness in $[S_{10}]$ computed by linearly interpolating the dataset in Figure 3.9, s_{pix} is the telescope pixel scale in $\left[\frac{\text{arcsecond}}{\text{pix}} \right]$, and Δt is the integration time in seconds. Note the addition of the 10^{-4} factor to reconcile catalog surface brightness in terms of 10th magnitude stars, and the 0th magnitude source in BINT. This

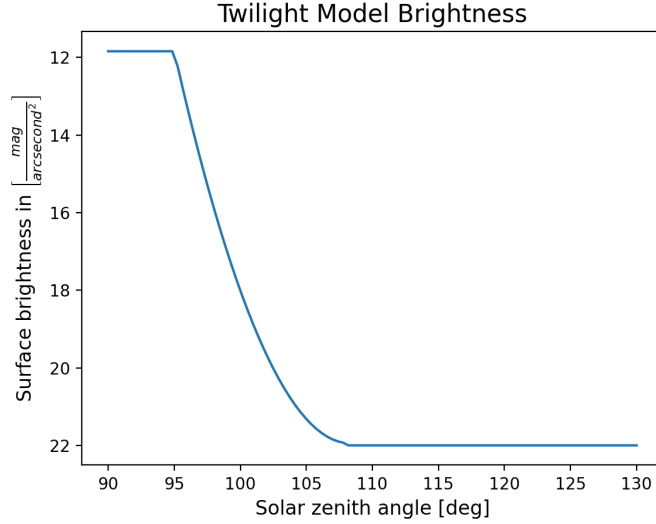


Figure 3.6. Twilight model surface brightness at zenith as a function of solar zenith angle

yields \bar{S}_{star} with units $\left[\frac{e^-}{pix^2}\right]$; photoelectron counts (ADU) per pixel. Figure 3.10 shows the background signal mean due to integrated starlight.

Scattered Moonlight

Moonlight scattering through the atmosphere significant increases background brightness [9]. This scattering effect can be decomposed into Rayleigh (isotropically distributed) and Mie (exponentially distributed) scattering modes. The Rayleigh scattered component is computed with Table 4 published by Daniels parameterized by the angle from the observation to zenith z_{obs} , the angle from the Moon to zenith z_{moon} , and the angle between the observation and the Moon on the horizon ΔAz [53]. Interpolating this table yields the intensity of the Rayleigh scattering F_{rs} in $10^{-10} W/(cm^2 \cdot \mu m \cdot sr)$ [9]. The Mie scattered component is formulated with Eq 3.9.

$$F_{ms}(\lambda) = a_1 \left[e^{-\left(\frac{\Psi}{\Psi_1}\right)} + a_2 e^{-\left(\frac{\pi - \Psi}{\Psi_2}\right)} \right] F_{rs}(\lambda) \quad (3.9)$$

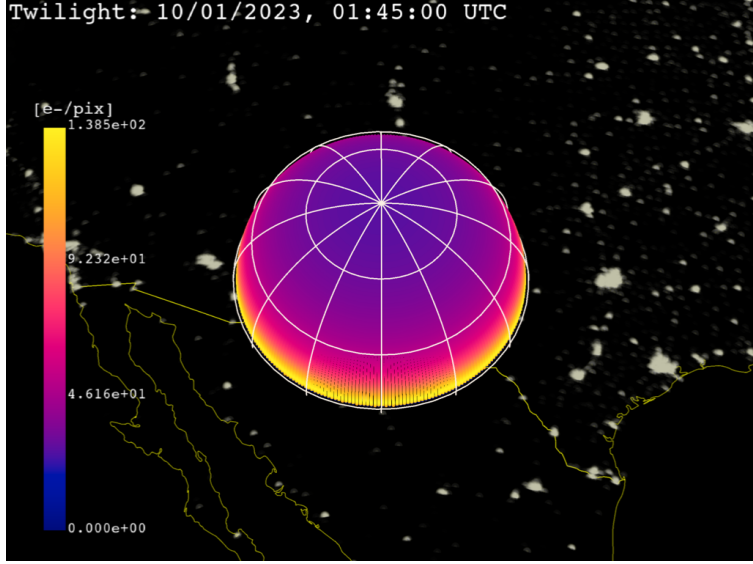


Figure 3.7. Mean twilight signal on the local observer hemisphere. The observer is in New Mexico, USA at 32.900° N , -105.533° W

Daniels recommends $a_1 \in [50, 100]$, $a_2 \in [0.01, 0.02]$, $\Psi_1 \in [10^\circ, 20^\circ]$, and $\Psi_2 \approx 50$ [53]. Prior to any station-specific fitting, the middle of these intervals are chosen, yielding $a_1 = 75$, $a_2 = 0.015$, $\Psi_1 = 15^\circ$, and $\Psi_2 = 50^\circ$. a_1 and a_2 are dimensionless, such that F_{ms} also has units of $10^{-10} \text{ W}/(\text{cm}^2 \cdot \mu\text{m} \cdot \text{sr})$. The total intensity of the scattered moonlight F_{mt} via Eq 3.10 following Krag's formulation [9].

$$F_{mt} = f(\theta) [F_{rs}(\lambda) + F_{ms}(\lambda)] \quad (3.10)$$

in Eq 3.10, $f(\theta)$ is the lunar phase function which describes the fraction of the full Moon brightness is reflected at an observer when the Sun-Moon-observer angle is θ . This function is linearly interpolated within Table 3 in [53]. Finally, Krag introduces a correction factor f_{corr} to account for the difference between the Sun's irradiance spectrum and the spectrum of scattered moonlight, defined in Eq 3.11.

$$f_{corr} = \frac{I_0}{SUN(550 \text{ [nm]})} \quad (3.11)$$

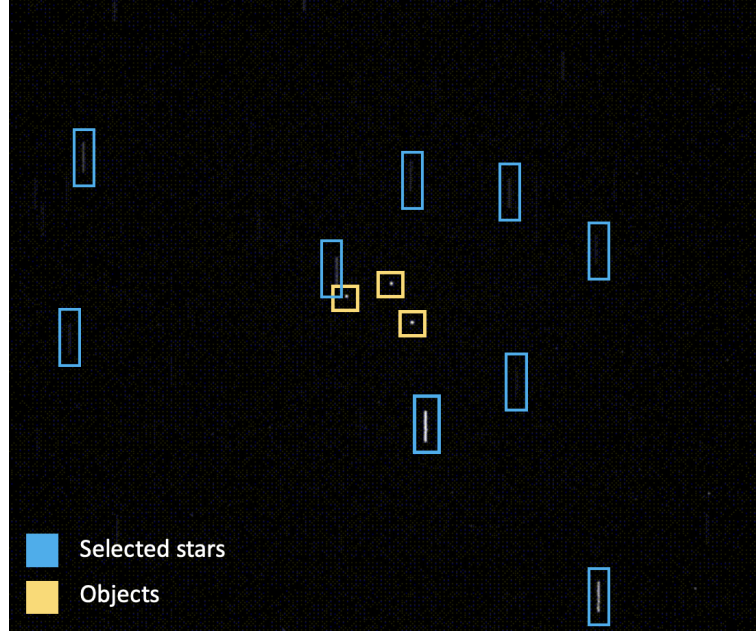


Figure 3.8. Raw image of three GEO objects with stars streaking through the background. As expected the star signals have a variety of signal-to-noise ratios. Taken by the Purdue Optical Ground station at 32.900° N, -105.533° W by Nathan Houtz.

With all these pieces, the mean scattered moonlight signal in ADU per pixel is computed in Eq 3.12.

$$\bar{S}_{moon} = F_{mt}(550 \text{ [nm]}) \cdot SINT \cdot \left(\frac{s_{pix}}{3600} \right)^2 \cdot \Delta t \cdot f_{corr} \quad (3.12)$$

Zodiacal Light

Zodiacal light is an effect created by sunlight reflecting off of dust in the ecliptic plane [9]. Zodiacal light is strongest around the Sun — an exclusion zone for most optical telescopes — but also reaches a peak directly away from the Sun due to the opposition effect. This peak is known as the Gegenschein, meaning "opposing light". The zodiacal light brightness is linearly interpolated within Table 1 of [54] which is listed for convenience in Appendix

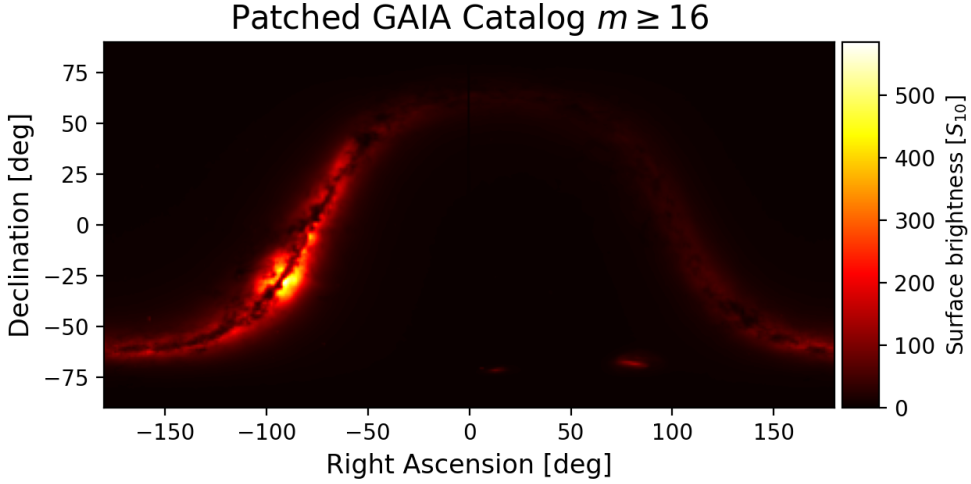


Figure 3.9. Integrated starlight brightness map

7.1.1. This reports the surface brightness of the zodiacal light in S_{10} , which is used without conversion to find the mean CCD signal in ADU per pixel via Eq 3.13.

$$\bar{S}_{zod} = BINT \cdot \left(\frac{s_{pix}}{3600} \right)^2 \cdot \Delta t \cdot ZOD \cdot 10^{-4} \quad (3.13)$$

As in the integrated starlight signal, the 10^{-4} factor reconciles the S_{10} surface brightness with the 0th magnitude source in BINT.

Background Sampling

The background signals are only defined in terms of their means, as each signal models the expected amount of radiation without accounting for the quantized nature of light [9]. Since light is transmitted in individual photons, their incidence on a given pixel will follow a statistical distribution. Assuming that each photon does not interact with others, the

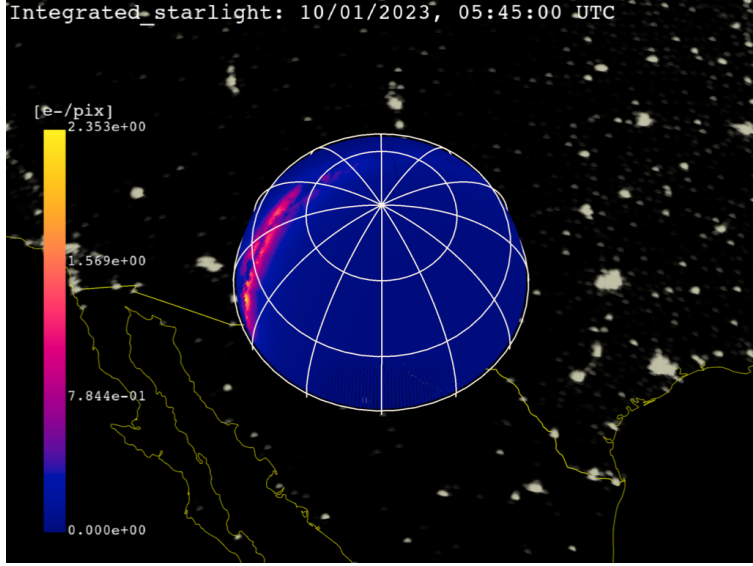


Figure 3.10. Integrated starlight signal on the local observer hemisphere. The observer is in New Mexico, USA at 32.900° N, -105.533° W

incidence of a photon on a pixel is well-modeled as a Poisson process for each background term [4]. This distribution models the number of independent and identically distributed events that occur during a time period. For CCD astronomy, this translates to the event of a photon hitting the sensor. A Poisson distribution is defined on the positive integers by a single parameter λ which is both the mean and variance of the distribution. The probability density function (PDF) for the Poisson distribution takes the form of Eq 3.14 [4].

$$P_{\lambda}(x = k) = \frac{\lambda^k e^{-\lambda}}{k!} \quad (3.14)$$

This distribution has a useful property that $P_{\lambda_1+\lambda_2}(x = k) = P_{\lambda_1}(x = k) + P_{\lambda_2}(x = k)$ so long as the distributions described by λ_1 and λ_2 are independent. Our background sources are reasonably assumed to be independent as they each originate from distinct physical processes.

$$\lambda_{background} = \bar{S}_{airglow} + \bar{S}_{pollution} + \bar{S}_{twilight} + \bar{S}_{star} + \bar{S}_{moon} + \bar{S}_{zod} \quad (3.15)$$

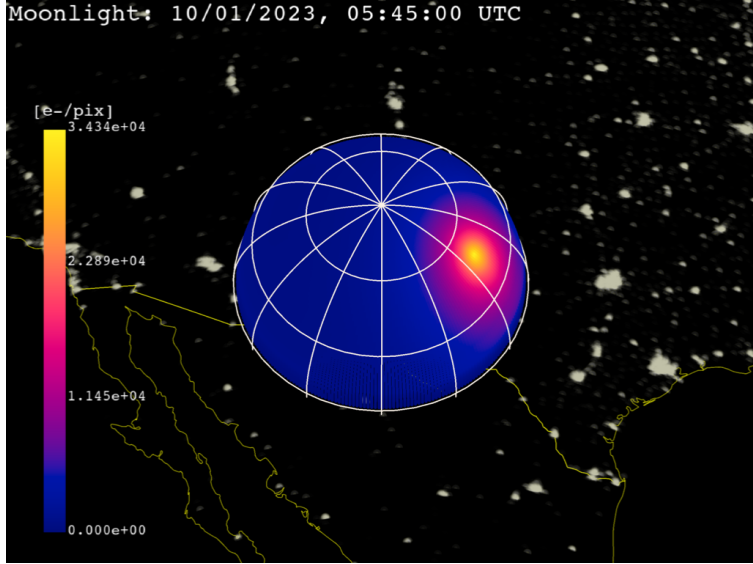


Figure 3.11. Mean scattered moonlight signal on the local observer hemisphere. The observer is in New Mexico, USA at 32.900° N, -105.533° W

Drawing samples from the Poisson distribution defined by $\lambda_{background}$ computes the background of the CCD image.

3.1.3 Sensor Effects

Dark Noise

The dark noise, also called the dark current or dark count, captures the temperature-dependent accumulation of electrons in the CCD pixel wells [9]. This noise source is modeled as a Poisson process with parameter λ_{dark} [4] and is assumed to be independent from the other sensor effects. This source accumulates with the integration time, giving it units of counts per second [9].

Readout Noise

When the CCD is read out, the charge contained in each pixel well must be digitized. This process introduces noise in the final signal due to electronic effects within the CCD circuitry and its surrounding environment [9]. The readout noise is modeled as a zero-mean

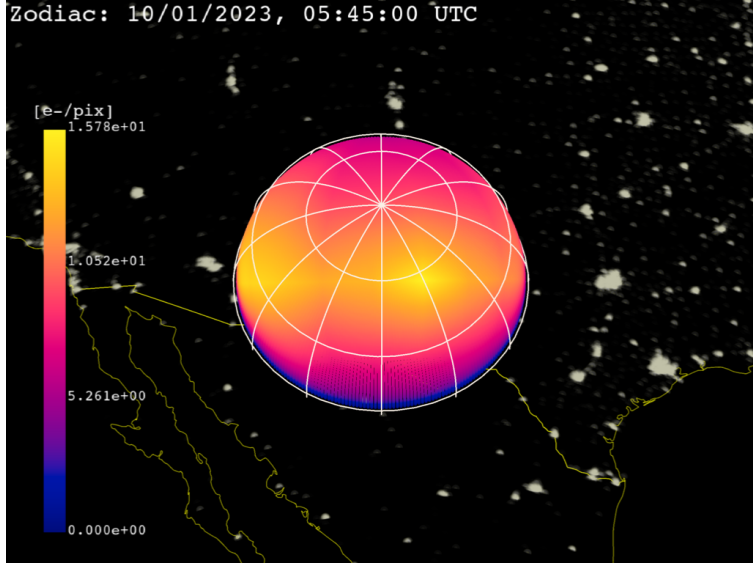


Figure 3.12. Mean zodiacal light signal on the local observer hemisphere. The observer is in New Mexico, USA at 32.900° N, -105.533° W

Gaussian distribution with variance σ_{read}^2 and is also assumed to be independent from other sensor effects [4].

Truncation Noise

Truncation noise in a CCD stems from the fact that the charge in each pixel is digitized into an integer factor of the gain [4]. This is modeled using a uniform distribution on $[-g/2, g/2]$, yielding a variance $N_{trunc}^2 = \frac{g^2}{24}$ [4].

3.1.4 Signal-to-Noise Ratio (SNR)

Because the unresolved object signals are always superimposed on the background of the image, the SNR of a CCD is expressed with the signal included in the denominator noise term [4]:

$$SNR = \frac{S_{obj}}{\sqrt{S_{obj} + N}}. \quad (3.16)$$

Explicitly, the SNR can be expanded in terms of the signal means and variances [4]:

$$SNR = \frac{S_{obj}}{\sqrt{S_{obj+n_{pix}}(\lambda_{background} + \lambda_{dark} + \sigma_{read}^2 + \frac{g^2}{24})}}. \quad (3.17)$$

3.2 Light Curve Simulation

3.2.1 Orbital Dynamics

TODO

3.2.2 Discrete Shape Representations

A computer can represent 3D objects implicitly or explicitly. An implicit representation might be the solution to an algebraic equation, i.e., $x^2 + y^2 + z^2 = 1$ defines a sphere of radius 1 centered at the origin. Often, a shape may be defined by a set of signed distance functions (SDFs). An SDF takes in a point in \mathbb{R}^3 and outputs the distance from the object, returning negative distance if the queried point is inside the shape. The object can then be rendered via ray marching. A ray is cast from the camera out into the scene for each pixel of the screen, each performing distance queries along its length until it intersects the object or diverges.

By contrast, an explicit shape representation creates complex 3D geometry from simple 2D building blocks. In the most common case, object faces are defined by triangles. This means that at the scale of the individual faces, the shape is always composed of flat surfaces that meet at sharp angles. While this can add complexity to many fields of shape analysis and geometry processing, triangulated surfaces are perfect for our application. Human-made space objects like most satellites are composed of flat faces, with the exception of parabolic antennas and cylindrical rocket bodies.

The Object File Format

One common text file format for 3D model files is `.obj`, developed by Wavefront Technologies in the early 1990s [55]. Each OBJ file consists of a list of vertex positions and face definitions, with optional vertex normals and tangents. An `.obj` listing for a cube is included for reference in Appendix 7.1.3. Given the vertex positions and adjacency information stored in the model file, useful properties of the object can be computed for use later in both light curve simulation and shape inversion.

Properties of Triangulated Meshes

For each triangular face F_i of the model defined by vertices $F_i = \{v_1, v_2, v_3\}$, the outward-pointing face normal is computed with

$$\hat{n} = \frac{(v_2 - v_1) \times (v_3 - v_1)}{\|(v_2 - v_1) \times (v_3 - v_1)\|_2}. \quad (3.18)$$

The face area is computed with

$$a = \frac{\|(v_2 - v_1) \times (v_3 - v_1)\|_2}{2}. \quad (3.19)$$

The support of the i th face — the perpendicular distance from the origin to the plane defining the face — is computed with the position of any vertex on that face, i.e., the first vertex $v_{i,1}$, and the face normal vector \hat{n}_i

$$h_i = v_{i,1} \cdot \hat{n}_i. \quad (3.20)$$

The volume of the object is computed with

$$V = \frac{1}{3} \sum_{i=0}^{|F|} \vec{h}_i \cdot \vec{a}_i. \quad (3.21)$$

In Eq 3.21, $|F|$ is the number of faces defining the object. \vec{h} and \vec{a} are column vectors collecting all face supports and areas. The Extended Gaussian Image, a quantity defined in 3.3.1, is computed row-wise for the i th face with

$$\vec{E}_i = \vec{a}_i \vec{n}_i. \quad (3.22)$$

3.2.3 Selected Satellite Models

Most of the analysis in this work used one of the 3D model files shown in Figure 3.13. Figure 3.13 highlights the size of the GEO communications satellites (TELSTAR, HYLAS, Hispasat, and ASTRA). In contrast, the LEO satellites (Starlink and Landsat) are dwarfed at the left end of the lineup.

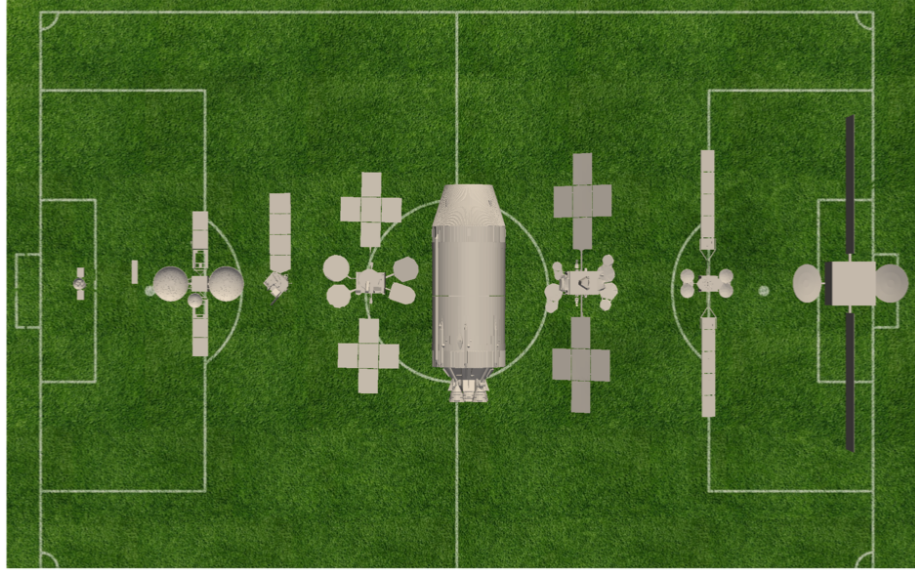


Figure 3.13. Selected space objects with soccer field for size reference. In order, the objects are TESS, Starlink V1, TDRS, Landsat 8, Hispasat 30W-6, Saturn V SII, TELSTAR 19V, HYLAS 4, and simplified ASTRA.

3.2.4 The Bidirectional Reflectance Distribution Function

Although light curves come from unresolved measurements, the interactions that produce them are directly driven by the shape and material properties of the object being observed. In order to simulate accurate light curves, all relevant optical interactions must be modeled. In broad terms, this boils down to determining how the object is illuminated, how it casts shadows on itself, and how it is observed.

At the microscopic scale, the surface of an object is composed of facets — small areas sharing a normal vector. The macroscopic optical properties of the material is driven by the distribution of sizes and normal directions of these microfacets. If the facet normals are distributed in biased orientations, the macroscopic surface may show anisotropy, leading to the appearance of brushed metal. If the facets normals are at large angles to each other, the

surface may appear dull as the direction of the outgoing light may be largely independent from the incoming direction. Subsurface effects — where incoming light rays scatter *inside* the surface can also change the macroscopic properties of the material.

This discussion raises an important question; how should the macroscopic outcomes of the microscopic interactions of incident light on a surface be modeled? The bidirectional reflectance distribution function (BRDF) is a tool from computer graphics that addresses this problem. The BRDF is a function on the hemisphere which expresses the fraction of light per solid angle (radiance \mathcal{R}) leaving the surface in a given direction, divided by the incident power per unit area (irradiance \mathcal{I}). The general formulation for a BRDF f_r is given by Eq 3.23 [56].

$$f_r(\mathbf{x}, L \rightarrow O) = \frac{d\mathcal{R}(\mathbf{x} \rightarrow O)}{d\mathcal{I}(L \rightarrow \mathbf{x})} \quad (3.23)$$

In Eq 3.23, $\mathbf{x} \in \mathbb{R}^3$ is the point on the object's surface where the BRDF is evaluated. $L \in \mathbb{S}^2$ is the incoming illumination unit vector and $O \in \mathbb{S}^2$ is the outgoing unit vector. Note that this work treats $f_r(\mathbf{x}, L \rightarrow O)$ and $f_r(L \rightarrow O)$ as equivalent in later descriptions, leaving the evaluation point \mathbf{x} implied. This definition is useful for building intuition about the form of the BRDF, but to represent a physically plausible reflection process, a candidate function must satisfy three additional constraints. A physically plausible BRDF must conserve energy — more energy cannot be reflected from the surface than was incident on it. It must also be reciprocal — switching the observer and illumination directions should not change the BRDF value as the surface interaction. This reciprocity is sometimes known as the *Helmholtz Reciprocity Rule* in literature [57]. Finally, plausible BRDFs are positive — they take on nonnegative values for all valid inputs [57]. A surface cannot reflect negative light, so this should feel natural. Explicitly, energy conservation is expressed by Eq 3.24 [57].

$$\forall L \in \mathbb{S}^2 : \int_{O \in \mathbb{S}^2} f_r(L \rightarrow O) d\mathbb{S}^2 \leq 1 \quad (3.24)$$

Eq 3.24 states that for all possible illumination directions L , integrating all possible outgoing observer directions O on the unit sphere cannot return greater than one from the energy conservation integral. Reciprocity can also be formalized via 3.25.

$$\forall L, O \in \mathbb{S}^2 : f_r(L \rightarrow O) = f_r(O \rightarrow L) \quad (3.25)$$

3.2.5 BRDF Formulations

Now that the requirements for a plausible physical BRDF have been established, a collection of commonly-used BRDFs can be presented. The following BRDFs are all energy conserving, reciprocal, and nonnegative. This does not mean that they are always sufficient for modeling real-world materials, they merely represent ways hypothetical surfaces could reflect light without breaking any fundamental physics.

Lambertian

The simplest BRDF is one that reflects equally in all directions. This BRDF is termed Lambertian or diffuse.

$$f_r(L \rightarrow O) = \frac{C_d}{\pi} \quad (3.26)$$

In Eq 3.26, $0 \leq C_d \leq 1$ is the surface's coefficient of diffuse reflection. For example, $C_d = 0.4$ means that the surface reflects 40% of incident radiation and absorbs the other 60%.

Phong

While the diffuse BRDF reflects energy isotropically, many real-world reflections are highly biased. At the extreme end, a perfect mirror reflection is effectively a Dirac delta function in the reflected illumination direction. Many real-world materials are well-modeled as a linear combination of diffuse and specular effects. A simple specular BRDF model is that developed by Phong in 1975 [58]. The Phong model splits the BRDF into a Lambertian term governed by C_d and a specular term governed by the coefficient of specular reflection $0 \leq C_s \leq 1$ and the specular exponent $n \geq 0$ [56].

$$f_r(L \rightarrow O) = \frac{C_d}{\pi} + \frac{C_s \frac{n+2}{2\pi} (O \cdot R)^n}{N \cdot L} \quad (3.27)$$

In Eq 3.27, R is the reflected illumination vector, computed via $R = 2(N \cdot L)N - L$. As n increases, the specular glint becomes sharper and more intense, eventually approaching a perfectly mirror reflection. Because of the introduction of a new coefficient of reflection, a new constraint is needed to maintain energy conservation. Because C_d and C_s each represent the *fraction* of light reflected in each mode, it should be clear that $C_d + C_s \leq 1$. This can also be reformulated with an explicit coefficient of absorption C_a which captures the fraction of incident radiation absorbed by the surface, yielding $C_d + C_s + C_a = 1$.

Blinn-Phong

The Blinn-Phong BRDF is similar to the Phong BRDF, but parameterizes the specular lobe in terms of the halfway vector H [56]. This vector is halfway between the illumination and observer directions such that $H = L + O$ which needs to be normalized before use. As the halfway vector approaches the surface normal vector, the observer must be approaching the reflected illumination vector, leading to a more intense specular highlight.

$$f_r(L \rightarrow O) = \frac{C_d}{\pi} + \frac{C_s \frac{n+2}{2\pi} (N \cdot H)^n}{4(N \cdot L)(N \cdot O)} \quad (3.28)$$

Glossy

The so-called glossy BRDF simulates reflections from plastic materials using a Gaussian distribution around the specular scattering lobe [56]. In Eq ??, the parameter σ controls the width of the specular Gaussian.

$$f_r(L \rightarrow O) = \frac{C_d}{\pi} + \frac{C_s}{2\pi\sigma^2(N \cdot L)} e^{-\frac{(R \cdot O)^2}{2\sigma^2}} \quad (3.29)$$

Cook-Torrance

The Cook-Torrance explicitly accounts for the orientation of the microfacets making up the surface [59]. This model is built from a facet slope distribution term D , a Fresnel term F , and a geometric attenuation factor G . The slope distribution term describes the probability density of a given facet being oriented with a normal vector aligned with the halfway vector H [59]. A common formulation of this term is due to Beckmann:

$$D = \frac{1}{\pi\alpha^2(N \cdot H)^4} \exp\left(\frac{1 - (N \cdot H)^2}{\alpha^2(N \cdot H)^2}\right). \quad (3.30)$$

In Eq 3.30, $\alpha \in [0, 1]$ is the roughness of the surface [59]. The Fresnel term accounts for the variation in specular reflection due to the angle of incidence. In reality, this term is a function of wavelength, but is often approximated as [59]:

$$F = C_s + (1 - C_s)(1 - (H \cdot L))^5. \quad (3.31)$$

The geometric attenuation term expresses how microfacets shadow each other, and can be approximated with [59]:

$$G = \min\left\{1, \frac{2(N \cdot H)(N \cdot O)}{O \cdot H}, \frac{2(N \cdot H)(N \cdot L)}{O \cdot H}\right\}. \quad (3.32)$$

The overall reflectance for the Cook-Torrance BRDF is given by:

$$f_r(L \rightarrow O) = \frac{C_d}{\pi} + \frac{D \cdot G \cdot F}{4(N \cdot L)(N \cdot O)} \quad (3.33)$$

Oren-Nayar

The Oren-Nayar BRDF is an improved model of diffuse reflectance for many real-world materials like ceramics and the surface of the Moon. These materials diverge from the Lambertian model near the horizon, reflecting much more light than would be predicted by simple cosine loss [60]. This BRDF relies on the surface roughness α to compute a set of constants [60]:

$$\begin{aligned}
A &= 1 - 0.5 * \frac{\alpha^2}{\alpha^2 + 0.33} \\
B &= 0.45 * \frac{\alpha^2}{\alpha^2 + 0.09} \\
C &= \frac{\text{proj}_N(L)}{\|\text{proj}_N(L)\|} \cdot \frac{\text{proj}_N(O)}{\|\text{proj}_N(O)\|} \\
\beta &= \max \{ \arccos(L \cdot N), \arccos(O \cdot N) \} \\
\gamma &= \min \{ \arccos(L \cdot N), \arccos(O \cdot N) \}
\end{aligned} \tag{3.34}$$

With these values computed, the reflectance of the Oren-Nayar BRDF is given by [60]:

$$f_r(L \rightarrow O) = \frac{C_d}{\pi} (A + (B \max \{C, 0\} \sin \beta \tan \gamma)) \tag{3.35}$$

Ashikhmin-Shirley

The Ashikhmin-Shirley BRDF is unique among those presented in this section as it allows for anisotropic reflection which can be non-negligible for metals [61]. This model is parameterized by the diffuse reflection coefficient, as well as two specular exponents n_u and n_v . When $n_u = n_v$, the model behaves much like the Phong BRDF. The full BRDF is expressed [61]:

$$\begin{aligned}
\rho_d &= \frac{28C_d}{23\pi} (1 - C_s) \left(1 - \left(1 - \frac{N \cdot L}{2} \right)^5 \right) \left(1 - \left(1 - \frac{N \cdot O}{2} \right)^5 \right) \\
\rho_s &= \frac{\sqrt{(n_u + 1)(n_v + 1)}}{8\pi} \frac{(N \cdot H)^{\frac{n_u(H \cdot U)^2 + n_v(H \cdot V)^2}{1 - (H \cdot N)^2}}}{(H \cdot L) \max \{N \cdot O, N \cdot L\}} F
\end{aligned} \tag{3.36}$$

$$f_r(L \rightarrow O) = \rho_d + \rho_s.$$

In Eq 3.36, F is the same Fresnel factor in Eq 3.31 while U and V are predefined surface basis vectors perpendicular to the surface normal.

3.2.6 BRDF Summary

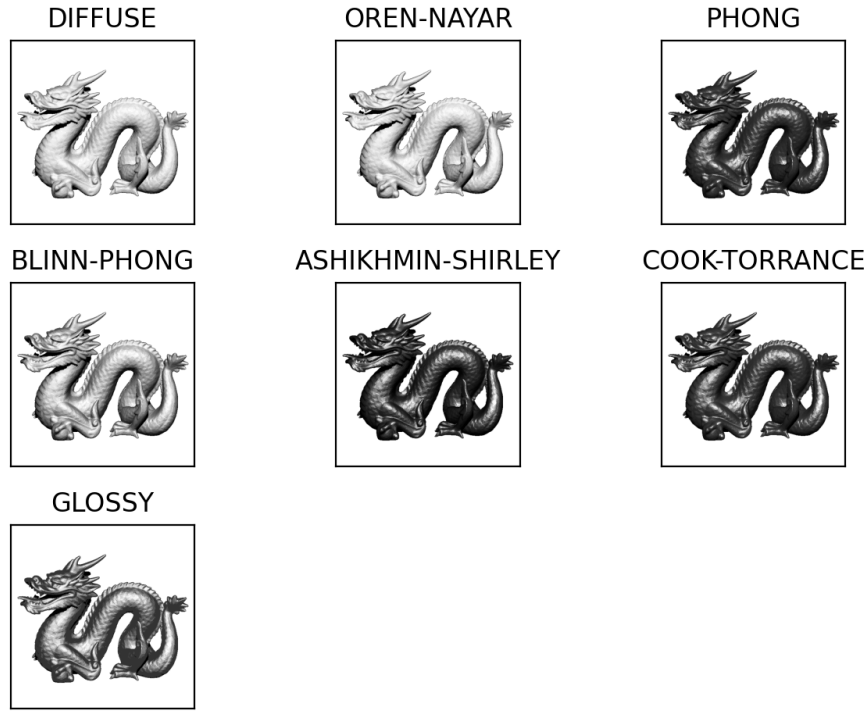


Figure 3.14. Implemented BRDFs rendered with arbitrary parameters, demonstrating the qualitative differences between lighting models

3.2.7 Simulating Light Curves for Convex Objects

Light curve simulation for convex geometry can be solved semi-analytically as each face's contribution to the measured irradiance can be computed individually [12]. Determining whether a face is illuminated requires two horizon checks to determine visibility from the Sun and to the observer. For a face i at timestep j these horizon checks are expressed by the shadowing condition μ_{ij} .

$$\mu_{ij} = \begin{cases} 1 & \text{if } (O_j \cdot \hat{n}_i) > 0 \text{ and } (L_j \cdot \hat{n}_i) > 0 \text{ and } \delta_{ij,ss} = 0 \text{ and } \delta_{ij,os} = 0 \\ 0 & \text{otherwise} \end{cases} \quad (3.37)$$

The unit vectors O and L point from the center of mass of the object to the observer and Sun, respectively. We choose the outward-pointing face normal unit vector \hat{n} by convention for all mesh operations. The self-shadowing and observer-shadowing conditions, $\delta_{ij,ss}$ and $\delta_{ij,os}$, are always zero for convex polyhedra but are crucial for accurately simulating nonconvex geometry. For objects with concavities, self-shadowing refers to shadows cast by an object onto itself and observer-shadowing refers to otherwise visible faces blocked by other portions of the geometry.

The irradiance I received by the observer at timestep j is the sum of the received irradiance from all faces, composed of specular and diffuse contributions. Each contribution is expressed as the product of the normalized irradiance \hat{I} . This can be scaled to adjust for the distance from the observer to the object to yield the noiseless received irradiance.

TODO: add $L = G_a$ stuff

3.2.8 Simulating Light Curves for nonconvex Objects

Many existing light curve simulation methods for nonconvex objects rely on ray tracing schemes like Möller and Trumbore's ray-triangle intersection algorithm [5], [62]. This computation has complexity $\mathcal{O}(n^2)$ if implemented naïvely, but can be improved to $\mathcal{O}(n \ln n)$ with better spatial data structures. For human-made space objects, there may be significant self-shadowing at large phase angles. As a result, it cannot be assumed that the self-shadowing conditions $\delta_{ij,ss}$ and $\delta_{ij,os}$ are zero [5], [39]. Naïve ray traced shadows generally require $\mathcal{O}(n^2)$ ray-triangle intersections per timestep for n faces. For this reason, ray traced shadows quickly become infeasible for complex objects without GPU parallelization. The limitations of ray-triangle intersections for light curve simulation is discussed at length by Frueh et al. [39].

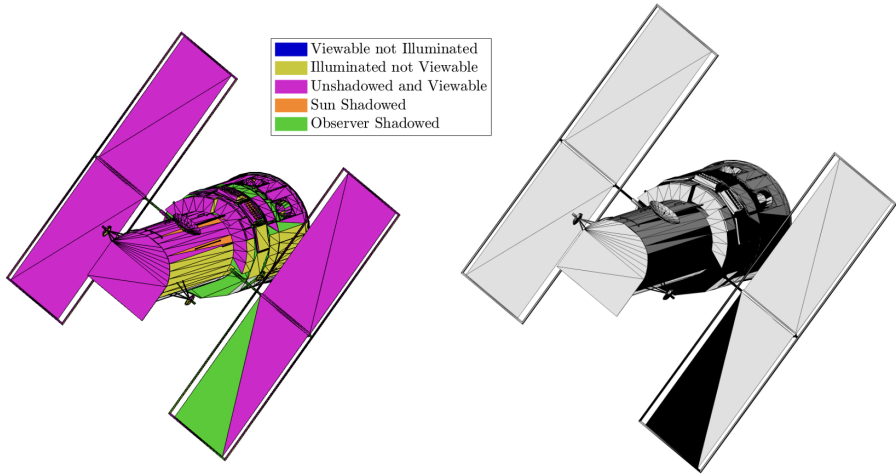


Figure 3.15. Hubble Space Telescope ray traced shadow categorization and shading. Models from [63]

3.2.9 The Importance of Self-Shadowing

To motivate the need for accurate shadows when dealing with human-made space objects, consider the error introduced by neglecting shadows for different types of space objects. Kaasalainen and Torppa's work on asteroids reasonably assumed that shadowing was a negligible contribution to the measured light curve. Human-made objects do not afford the same luxury. Figure 3.16 displays light curves for the asteroid Bennu and the Hubble Space Telescope with and without accurate shadows under a single-axis spin profile with inertially fixed Sun and observer vectors. Without accurate shadowing, the light curve's intensity and its time derivative can be significantly error-prone.

3.2.10 Shadow Mapping

TODO: remake 3.17 with figure from Python.

In the LightCurveEngine, shadow mapping is used for faster and more accurate self-shadowing. Shadow mapping is a well understood technique in computer graphics [64]. Although modern ray traced shadowing may be more computationally efficient, shadow mapping was selected for its ease of implementation [64]. Because shadow mapping shades

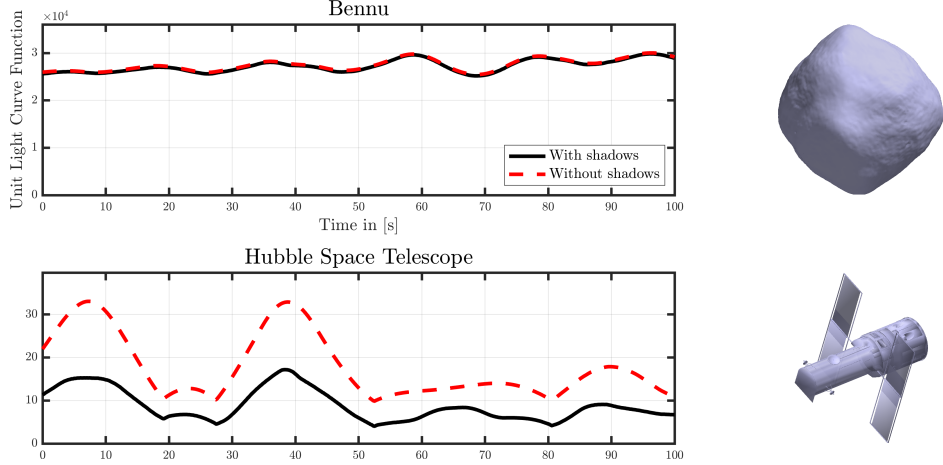


Figure 3.16. Brightness errors introduced by neglecting shadows for Bennu and HST. Models from [63]

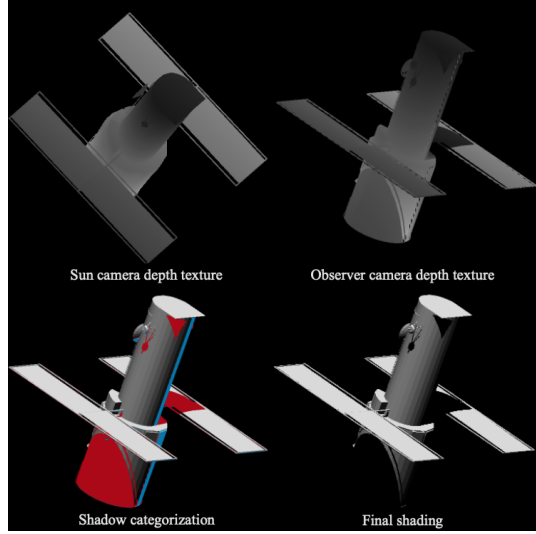


Figure 3.17. Hubble Space Telescope shadow mapping with self (red) and horizon (blue) shadows rendered. Models from [63]

individual pixel fragments instead of entire faces, it offers increasing shadow quality over facewise ray tracing as the number of mesh faces falls.

Given an observer and Sun vector in the body frame of the object, shadow mapping proceeds in a four step process. In step one, a camera is positioned along the Sun vector and a perpendicular depth texture is computed. In the second step, depth values in Sun

camera space are transformed to observer camera space, where a second depth texture is computed. This second texture is used to find the closest fragment along each ray to the Sun [65]. Self-shadowed fragments are classified as those further from the Sun than the closest fragment along the same ray, indicated in red in Figure 3.17. Fragments that do not pass the convex shadowing condition are horizon shadowed, indicated in blue in Figure 3.17, determining the Sun and observer shadowing conditions at once. All remaining fragments are shaded with using the same Lambertian reflection model in ?? TODO: this equation is broken. Computing the light curve function for the final rendered image requires summing all pixel values and dimensionalizing the result by the area of the observer camera's field of view. The light curve simulation environment used in this work was implemented in C and OpenGL using raylib [66].

TODO: add algorithm pseudocode for lighting shader

3.2.11 Sampling Noisy Light Curves

Given the irradiance of the object observed by the telescope, the noisy light curve is computed by building a grid containing the object signal, background noise, and sensor noise. On a pixel-by-pixel basis, the mean object signal is given by an alteration of Eq 2.33:

$$C_{obj}(x, y) = \frac{0.838\bar{C}_{all}}{2\pi\sigma^2} \exp\left(-\frac{(x - x_0)^2 + (y - y_0)^2}{2\sigma^2 s_{pix}^2}\right). \quad (3.38)$$

In Eq 3.38, (x_0, y_0) are the exact pixel coordinates of the object centroid, σ is the Gaussian standard deviation from Eq 2.32 in arcseconds, and s_{pix} is the pixel scale in arcseconds per pixel. Likewise, the total noise sampled in each pixel is given by samples from all the relevant source distributions:

$$C_{noise}(x, y) = N_{background} + N_{dark} + N_{trunc} + N_{read}. \quad (3.39)$$

In Eq 3.39, $N_{background}$ is a sample drawn from $\text{Pois}(\lambda_{background})$, N_{dark} is drawn from $\text{Pois}(\Delta t \lambda_{dark})$, N_{trunc} is drawn from $\text{Uniform}(-g/2, g/2)$, and N_{read} is drawn from $\text{Normal}(0, \sigma_{read}^2)$.

3.3 Light Curve Shape Inversion

3.3.1 Direct Convex Shape Inversion

Traditionally, direct light curve inversion involves two distinct optimization problems: a linear least squares problem to fit an EGI to the measured light curve, and a second optimization to produce accurate vertex positions and face adjacency information [5]. The first problem is data-driven and linear, using the observations to estimate a plausible EGI. The second problem is highly nonlinear but convex and requires significant tuning for robust convergence [21].

The Extended Gaussian Image

The discrete EGI $\vec{E} \in \mathbb{R}^{m \times 3}$ is composed of m unit vectors \hat{n} each scaled a nonnegative scalar $a \in \mathbb{R}$, $a_i \geq 0$ [14].

$$\vec{E}_i = a_i \hat{n}_i \quad (3.40)$$

In the context of shape inversion, the m vectors \hat{n} should be a relatively uniform tessellation of the unit sphere. A convex polytope can be uniquely represented by an EGI of facet normal vectors scaled by each facet's area. The set of normal vectors in an EGI is denoted \mathcal{N} with the set of areas denoted \mathcal{A} . The vector of facet areas is denoted $\vec{a} \in \mathbb{R}^{m \times 1}$. The norm of the EGI is notated $\|\vec{E}\| = \vec{a}$ with the ‘size’ of the EGI $\|\vec{E}\| = m$.

The solution to the Minkowski problem proves the existence and uniqueness of a convex polytope for any EGI satisfying the closure condition in Eq 3.41 [13]. Equivalently, an EGI uniquely represents a closed, convex polyhedron — a polytope — with no open boundaries, up to a translation.

$$\sum_{i=1}^m a_i \hat{n}_i = [0, 0, 0] \quad (3.41)$$

While a given EGI uniquely represents a polytope, that same EGI could also be interpreted to be an infinite number of nonconvex and open geometries. An example of this extended family is depicted in Figure 3.18.

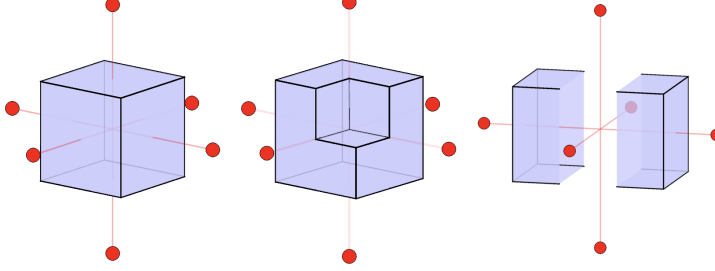


Figure 3.18. Simplified convex, nonconvex, and open EGI nonuniqueness. Larger circles indicate greater relative areas assigned to a given normal vector.

EGI Optimization

The EGI fulfills two important criteria for the shape inversion problem: it can be estimated directly from the light curve, attitude profile, and material properties, and uniquely represents a convex object [12]. Further, the EGI can be transformed into a unique convex object and vice versa through the dual transform and Minkowski problem [13], [67].

Given a light curve, direct shape inversion schemes sample m candidate normal vectors \hat{n} on the unit sphere to fit an EGI to the observed light curve $\vec{L}_{\text{ref}} \in \mathbb{R}^{n \times 1}$ [5], [23]. This is accomplished by solving an optimization problem to distribute the area vector \vec{a} across the sampled normals to minimize the residual between the observed and modeled light curves. In practice, this is a constrained nonnegative least squares (NNLS) problem and can be solved efficiently for large numbers of normal vectors and light curve data points:

$$\min_{\vec{a}} \|\vec{L}_{\text{ref}} - G\vec{a}\|_2 \quad \text{subject to } \vec{a}_i \geq 0. \quad (3.42)$$

NNLS problems are efficiently solved via Lawson and Hanson's original algorithm [68], or the more recent Fast NNLS (FNNLS) algorithm due to Bro and De Jong [69]. It is important to note that the area estimated with Eq 3.42 is necessarily *albedo-area* due to the diffuse reflectivity coefficient C_d in Eq. ???. If the value of C_d is uniform but unknown, the recovered geometry will incorrectly scaled without impacting the face adjacency or relative feature sizes.

The convex reflection matrix $G \in \mathbb{R}^{n \times m}$ with ijth entries G_{ij} defined at time i for each facet j is defined as the normalized received facet irradiance per unit facet area:

$$[g]_{ij} = \frac{I_{ij}}{I_0 a_j}. \quad (3.43)$$

This relationship between the object irradiance and area defines the normalized convex light curve \vec{L}_{convex} , that produced by a convex object of facet areas \vec{a} under the attitude profile and lighting conditions that yield G .

$$\vec{L}_{\text{convex}} = G \vec{a} \quad (3.44)$$

The optimization in Eq. 3.42 produces a coarse approximation of the true EGI as m is finite. Increasing m necessarily improves the quality and sparsity of the estimated EGI, but at the cost of computational resources. The estimation was performed using a synthetic light curve input from $n = 500$ Sun and observer vectors uniformly sampled on the sphere in the body frame, producing a full rank G matrix. $m = 500$ candidate normal vectors were sampled using a spherical Fibonacci mapping described by Keinert et al. in [70]. Results are visualized for an icosahedron in the body frame in Figure 3.19. Reconstructing the object at this stage is difficult due to the quantity of faces present in the estimated EGI.

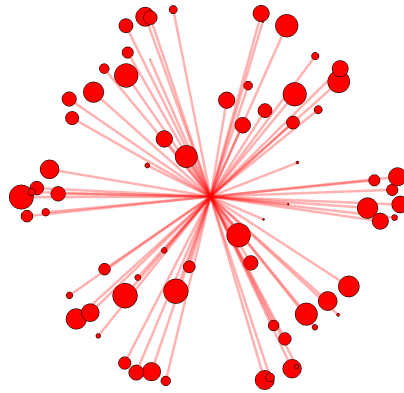


Figure 3.19. Initial icosahedron EGI optimization before resampling

TODO: re-do this figure with 2-sphere in python 3.19

EGI Resampling

We propose a normal vector resampling step to promote a more accurate and sparse EGI. The normal vectors used in Eq. 3.19 are generally correct, with each group clustering around a normal vector of the truth geometry. This clustering behavior occurs when none of the candidate normal vectors are sufficiently close to the truth. Resampling in a cone centered on each initial EGI normal vector provides more accurate candidates for EGI estimation. This process mimics a single optimization step with a much larger m , where the coarse EGI is used to exclude areas on the sphere with little or no normal area.

Uniformly sampling a cone of half-angle ϕ is accomplished by strategically sampling points on the unit sphere.

$$\hat{n}_{cone} = \begin{bmatrix} \sqrt{1-z^2} \cos \theta \\ \sqrt{1-z^2} \sin \theta \\ z \end{bmatrix} \quad (3.45)$$

In Eq. 3.45 two coordinates are chosen $z \in [\cos \phi, 1]$ and $\theta \in [0, 2\pi)$, yielding a point uniformly distributed on a cone of half-angle ϕ about the central axis $[0, 0, 1]^T$ [71]. These points are then rotated using a direction cosine matrix to center the cone on an axis of interest. The axis of rotation for this transformation is the cross product of the original central axis $[0, 0, 1]^T$ with the final axis \hat{n}_{cone} with the rotation angle θ being the angle between the same two vectors. This means that we can define the principal rotation parameter form of this transformation, which can be converted into the DCM using Eq 2.24 and 2.22, as

$$\begin{aligned} \theta &= \cos^{-1}(\hat{n}_{cone,z}) \\ \lambda &= \hat{n}_{cone} \times [0, 0, 1]^T. \end{aligned} \quad (3.46)$$

The number of new candidates sampled per initial solution vector and the cone half-angle should be adjusted on a case-by-case basis depending on the compute power available and light curve data quality. Multiple iterative methods exist for solving nonnegatively

constrained least squares (NNLS) problems. The classical NNLS algorithm was published by Lawson and Hanson and improved later by Bro and De Jong in their Fast NNLS (FNNLS) approach [68], [69].

Existing EGI optimization schemes like those of Fan [5], Friedman [23], and Cabrera [25] are limited by a single normal vector sampling step, leading to a lack of sparsity in the optimized EGI. High-density normal vector sampling in regions known to contain non-zero area leads to EGI solutions that are generally more sparse and cluster more tightly about true normal vectors.

This process is shown in Figure 3.20 for the same icosahedron with a half-angle $\phi = \frac{\pi}{20}$ and sampling density of 50 candidate vectors per cone.

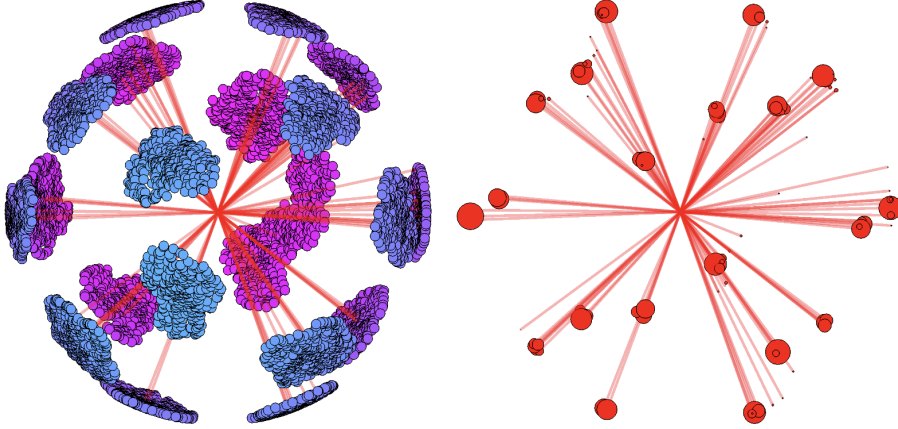


Figure 3.20. Resampled normal vectors (left) with reoptimized EGI (right)

TODO: remake this figure with 2-sphere

EGI Merging

After resampling and reoptimizing with Eq. 3.42, the reestimated EGI is merged by computing all groups \mathcal{G} of EGI vectors within an angular offset α :

$$\mathcal{G}_k = \left\{ \vec{E}_i \in \vec{E} \mid \cos^{-1} \left(\frac{\hat{E}_i \cdot \hat{E}_k}{\|\hat{E}_i\| \|\hat{E}_k\|} \right) < \alpha \right\}. \quad (3.47)$$

In practice, the choice of α is dependent on the user's tolerance for discretization, as merging will approximate smooth geometry by discrete faces with normal vectors offset by 2α . Groups are merged by summing all group members, yielding a single EGI vector \vec{E}_m without loss of closure.

$$\vec{E}_m = \sum_{\vec{E} \in \mathcal{G}_k} \vec{E} \quad (3.48)$$

Merging the resampled EGI using Figure ?? with $\alpha = \frac{\pi}{10}$ produces a final sparse EGI fit for object reconstruction, shown in Figure 3.21.

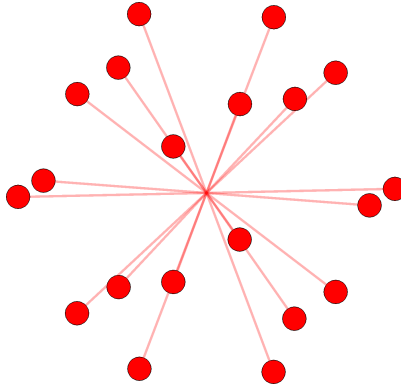


Figure 3.21. Merged icosahedron EGI

TODO: remake with true EGI on the right

Geometry Recovery from the EGI

At this stage, the resampled and merged EGI encodes a convex approximation of the underlying object with no guarantee of the closure of this EGI. The EGI closure constraint Eq. ?? motivates a simple procedure to correct an invalid EGI by adding the mean closure error to each entry:

$$\vec{E}_{\text{closed}} = \vec{E}_{\text{open}} - \sum_{i=1}^m a_i \hat{n}_i. \quad (3.49)$$

The concept of a closure step is not a novel contribution. Fan's method solved an problem to adjust the EGI towards closure [5]. This process is improved with a simpler analytical

correction. In practice, this process should be performed before each reconstruction to accelerate convergence. Failing to correct non-closed EGIs will cause convergence to a nonzero minimum in the reconstruction objective function as there is no corresponding convex object with the given EGI.

The unique convex object encoded by each closed EGI is reconstructed by solving for the polytope's set of vertices \mathcal{V} and faces \mathcal{F} encoding the adjacency relations between vertices. This is accomplished following the procedure introduced by Little through the dual transformation [14]. The dual set \mathcal{D} are vertices in $(A, B, C) \in \mathbb{R}^3$ that satisfy the following plane condition for a point (x, y, z) on each face of the object:

$$Ax + By + Cz + 1 = 0 \quad (3.50)$$

If (x, y, z) are chosen to be the closest points in the object's planes to the origin, the dual set \mathcal{D} can be expressed in terms of the EGI and a support vector $\vec{h} \in \mathbb{R}^{\|\mathcal{F}\| \times 1}$, as expressed in Eq 3.51. The support vector is the perpendicular distance of each face defining the object to the origin.

$$\mathcal{D} = \frac{\vec{E}}{\|\vec{E}\|\vec{h}} \quad (3.51)$$

The object's vertices \vec{v}_{ref} are found by solving a linear system of equations for each face on the convex hull of dual set vertices. Triplets of vertices on the resulting faces are used to find a single real vertex by intersecting the three planes defining the dual set vertices.

$$\begin{bmatrix} v_{ref,x} \\ v_{ref,y} \\ v_{ref,z} \end{bmatrix} = \begin{bmatrix} v_{i,x} & v_{j,x} & v_{k,x} \\ v_{i,y} & v_{j,y} & v_{k,y} \\ v_{i,z} & v_{j,z} & v_{k,z} \end{bmatrix}^{-1} \begin{bmatrix} 1 \\ 1 \\ 1 \end{bmatrix} \quad (3.52)$$

Convex face adjacency information is found by triangulating the convex hull of all reference vertices. The accuracy of the recovered geometry is entirely dependent on the correctness of the support vector \vec{h} used to produce the dual set. Finding the true support vector is the challenge of the final optimization in convex shape inversion.

Support Vector Optimization

Prior work by Fan used Little's objective function for support vector optimization [5], [14].

$$f(\vec{h})_{\text{Little}} = \vec{h} \cdot \vec{a} \quad (3.53)$$

TODO: description of the optimization

3.3.2 Direct nonconvex Shape Inversion

nonconvex Feature Detection and Location

Many human-made space objects are, as highlighted in Figure ??, highly nonconvex. As a result, their shape inversion is plagued by the fact that the Minkowski problem-driven reconstruction methods of Eq ?? cannot recover nonconvex features. Instead of beginning from the ground up, the convex shape guess can be leveraged to detect and locate concavities.

We can retain information about large, unilateral object concavities during EGI estimation in Eq. 3.42 by relaxing the EGI closure constraint. This unconstrained form is also generally functional for most convex objects and can be used without loss of detail in the final reconstruction as long as closure correction in Eq. 3.48 is still employed.

The mean axis of prominent concave features is determined by measuring the divergence of the optimized EGI from a closed object with the magnitude of the closure error \vec{e}_{EGI} .

$$\vec{e}_{EGI} = - \sum_{i=1}^m a_i \hat{n}_i. \quad (3.54)$$

The EGI closure error vector in Eq 3.54 represents the missing area on each body axis that could be added to close the object. The addition of the minus sign transforms the vector from expressing the presence of excess area to the absence of missing area. The closure error will be negligible if there are no concavities present. The closure error may also be negligible if there is no self-shadowing is present over the sampled attitude profile, therefore the closure error merely quantifies the self-shadowing that is occurring, not whether there may be self-shadowing in other orientations.

Under the strong assumption that the concavities present are major and unilateral, this EGI error vector points along the mean axis of the concavity.

TODO: replace this analytic relationship (which is bad and wrong) with an iteration to minimize LC error

Concavity Creation

Our process for creating an accurate concavity in the reconstructed convex guess proceeds in four major steps. The model is first subdivided to add more faces and vertices. Subdivided vertices are then classified by their proximity to the EGI error vector, indicating whether their positions should be updated. Boundary vertices are identified, and vertex positions are updated based on the estimated internal angle computed via Eq. ??.

Subdividing the initial convex object guess is essential for retaining object detail during concavity creation. A combination of linear subdivision, Loop subdivision, and remeshing algorithms are used to accomplish this. Linear subdivision is advantageous when object faces are equally sized and boundary edges must be maintained. Loop subdivision is preferable when there are numerous vertices so that subdivisions do not drastically diverge from the initial boundary surface. Loop subdivision softens sharp edges as it relies on B-splines to interpolate new vertex positions [72]. The specific type and resolution of subdivision used depends on the level of detail the user needs to maintain in the introduced concavity, although linear subdivision followed by Loop subdivision is a useful baseline. Varying combinations of subdivision are shown in Figure 3.22 to illustrate the available configurations.

When introducing a concavity, it is important to classify which vertices are part of the concave feature — and therefore need to be updated — and which vertices should remain unaffected. This is accomplished by measuring the angle from each face normal to the EGI error vector, where faces with normal vectors within an angle of $\pi/2$ to the error vector must be updated. In reality, all face normals and areas are impacted by the presence of the concavity in the area optimization Eq. 3.42 and EGI correction step Eq. 3.49. Selecting the angle deflect $\pi/2$ updates all faces above the horizon from the EGI error vector. This bound

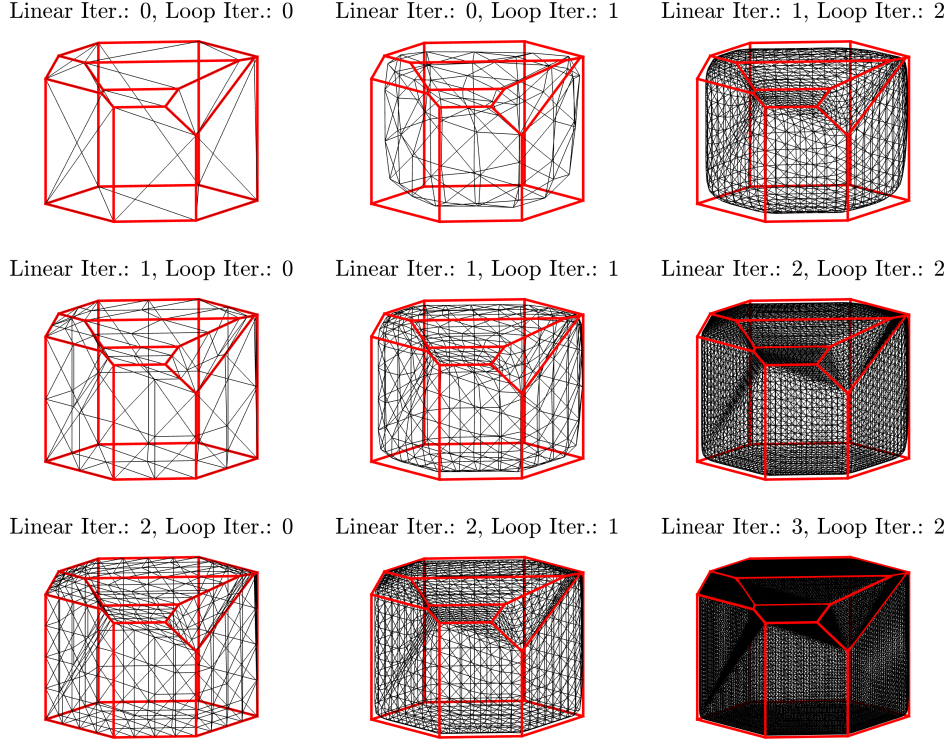


Figure 3.22. Subdivided object (black) with reference (red) with various levels of subdivision

tends to produce visually accurate concavities. Faces requiring an update are termed *free* faces, with all others termed *root* faces.

Vertices on free faces are further classified as being *root-adjacent* or *free*. Root-adjacent vertices are part of at least one root face, whereas free vertices belong to only free faces. Classifying vertices in this way results in a border of root-adjacent vertices around the interior free vertices, visualized in Figure 3.23.

Given the estimated internal angle ψ_{est} and the error vector $\hat{\mathbf{e}}_{EGI}$, each i th free vertex is displaced to introduce a geometrically accurate concavity by moving each a distance d_i in the direction of $-\hat{\mathbf{e}}_{EGI}$:

$$d_i = p_i \sqrt{\csc^2 \frac{\psi_{est}}{2} - 1}, \quad (3.55)$$

where p_i is the distance from each i th free vertex to the nearest root-adjacent vertex.

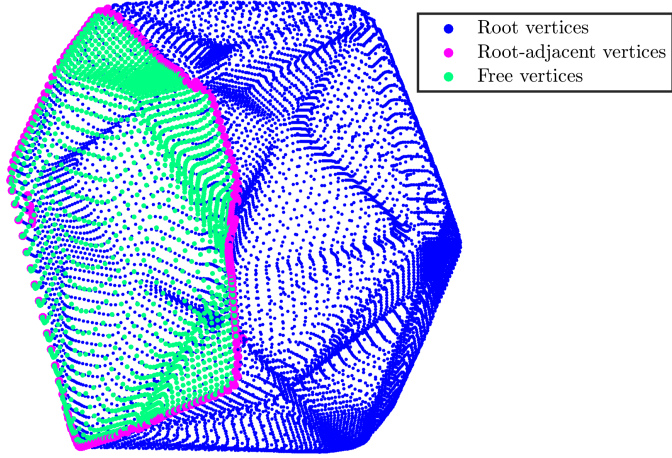


Figure 3.23. Root-adjacent and free vertices

3.3.3 Shape Inversion With Noisy Measurements

Shape Interpolation With Signed Distance Functions

The signed distance field (SDF) implicitly represents a shape by associating each point in \mathbb{R}^3 with the distance to the closest point on the surface of the object [73]. For a given SDF $f(x, y, z)$, the surface of the object is given by:

$$\begin{bmatrix} x \\ y \\ z \end{bmatrix} : f(x, y, z) = 0. \quad (3.56)$$

Computing the SDF of a triangulated mesh breaks down into computing distances from the points, line segments, and planes making up the mesh to the queried point [73]. A slice of the SDF of a test model is displayed in Figure 3.25.

Interpolating between two shapes can be accomplished through a weighted average of the respective SDFs. If both objects are weighted at 50%, the weighted sum of their SDFs produces a surface that lies halfway in between the two original shapes, measured perpendicular to the input objects' surfaces. This interpolated zero level set surface can be extracted through any three dimensional isocontouring algorithm such as marching cubes [74] or flying

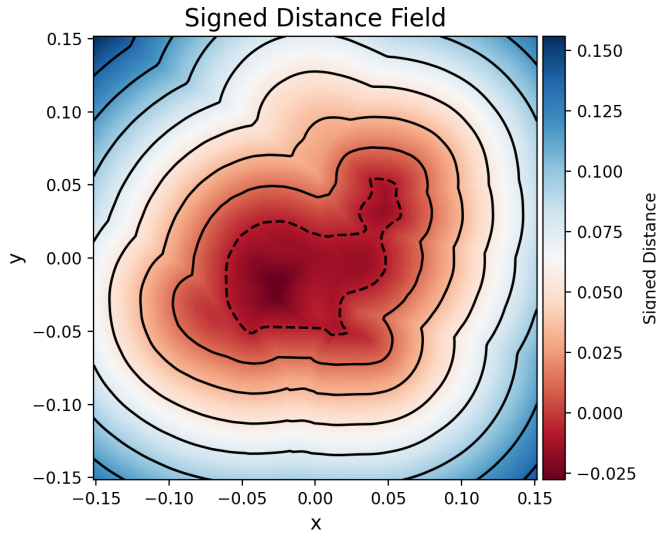


Figure 3.24. SDF slice of the Stanford bunny model

edges [75]. For example, interpolating between a torus and an icosahedron using this method yields Figure ??.

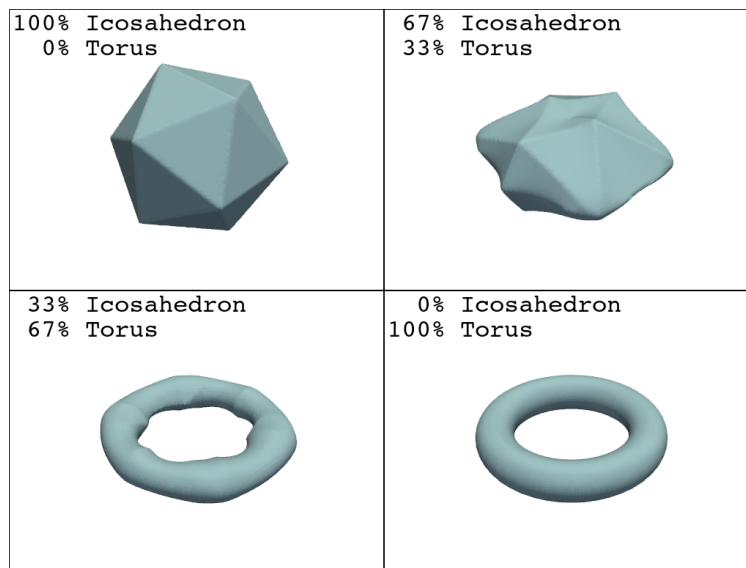


Figure 3.25. SDF interpolation between a torus and an icosahedron

$i \leftarrow 10$

if $i \geq 5$ **then**

```
i ← i - 1  
else  
    if i ≤ 3 then  
        i ← i + 2  
    end if  
end if
```

TODO: write

4. Results

4.1 Convex Shape Inversion Without Noise

TODO: this

4.2 nonconvex Shape Inversion Without Noise

Displacing free vertices in the EGI error vector direction by d_i yields accurate concavities for objects whose concave boundaries lie in a plane. The result of applying this process to a set of representative convex objects is shown in Figure 4.1 using the same attitude profiles and as in Figure ??.

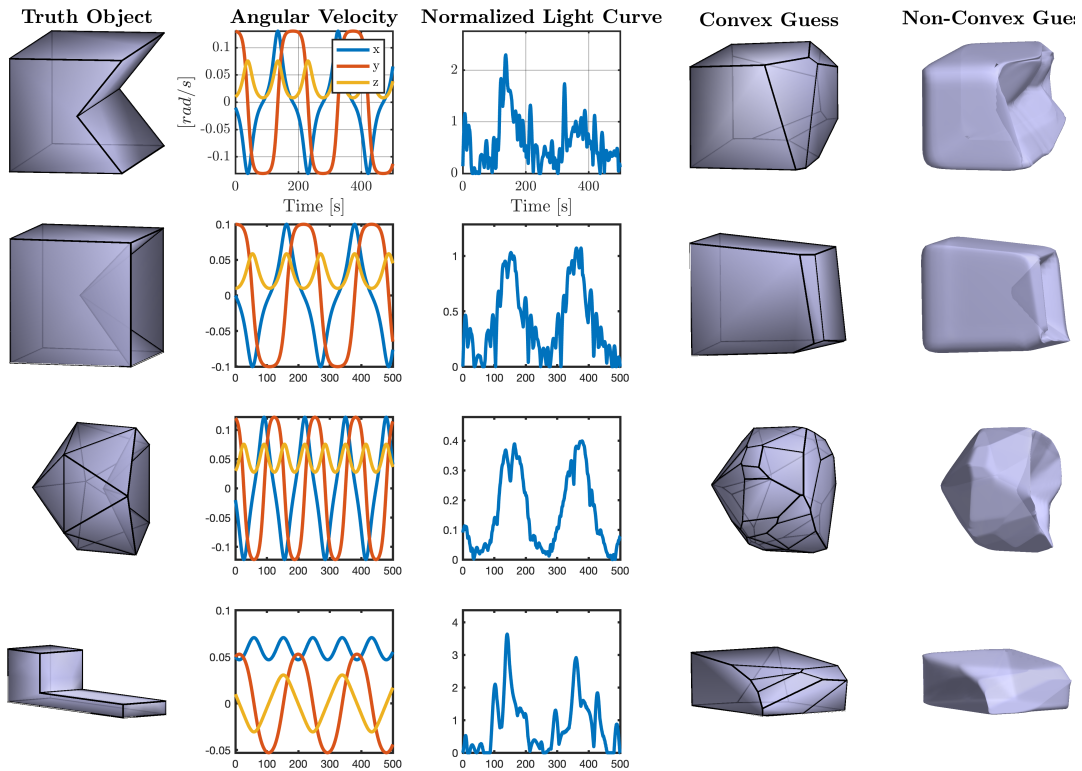


Figure 4.1. Collapsed house, cube, icosahedron, and box-wing satellite reconstructions using vertex displacement

The collapsed cube and icosahedron in Figure 4.1 are recovered effectively, but the collapsed house and box-wing satellite expose two limitations of the vertex displacement technique. In the case of the house where the concavity boundary is not constrained to a plane,

the edges of the created concave feature are incorrect. The box-wing satellite's shadowing geometry leads the convex guess to be a poor approximation of the geometry outside of the concavity while also inheriting the same problem as the house.

This vertex displacement scheme will negligibly impact the convex guess if the truth object is also convex. A convex truth object will produce a small $\|\vec{e}_{EGI}\|$, causing the vertex update depth d_i to trend towards zero as the estimated internal angle approaches $\psi = 180^\circ$. This is illustrated in Figure 4.2 using the same input convex objects and attitude profiles as in Figure ??.

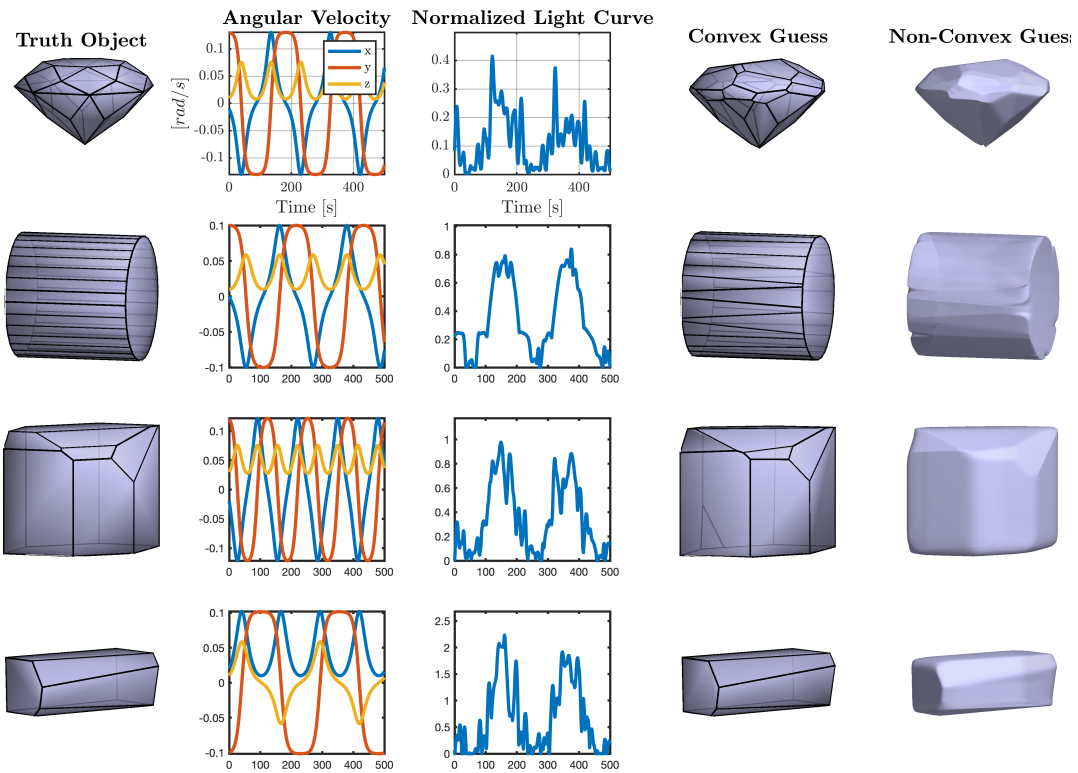


Figure 4.2. Convex objects under vertex displacement procedure

Figure 4.2 clearly displays the compatibility of vertex displacement with truly convex objects. All objects are reconstructed faithfully in both their convex and nonconvex inversions, with the same caveats noted in the discussion following Figure ???. Some truly sharp edges are rounded during mesh subdivision as seen in the gem or rectangular prism. That said, others like the cylinder become more accurate as subdivision reintroduces continuity lost to discretization in EGI merging.

4.3 Convex Shape Inversion With Noise

TODO: this

4.4 nonconvex Shape Inversion With Noise

TODO: this

5. Recommendations

6. Future Work

7. Appendices

7.1 Astronomical Spectra Data

Atmospheric Extinction

```
{"lambda": [0.0, 3.2e-07, 3.400000000000003e-07, 3.6e-07, 3.79999999999996e-07,
4e-07, 4.5e-07, 5e-07, 5.5e-07, 6e-07, 6.5e-07, 7e-07, 8e-07, 0.001], "extinction":
[5.0, 0.96, 0.54, 0.42, 0.34, 0.27, 0.17, 0.13, 0.11, 0.11, 0.07, 0.05, 0.03, 0.0]}
```

Quantum Efficiency

```
# Wavelength [nm], quantum efficiency [non-dim]
```

350.70422535211264e-9, 0.23880597014925387
361.9718309859155e-9, 0.27761194029850755
369.01408450704224e-9, 0.34925373134328375
378.8732394366197e-9, 0.37910447761194044
390.14084507042253e-9, 0.39104477611940314
398.59154929577466e-9, 0.41492537313432853
409.85915492957747e-9, 0.4477611940298508
419.71830985915494e-9, 0.43880597014925393
430.9859154929577e-9, 0.43880597014925393
439.4366197183098e-9, 0.4507462686567165
449.2957746478873e-9, 0.43880597014925393
459.15492957746477e-9, 0.43880597014925393
480.28169014084506e-9, 0.5134328358208956
488.7323943661972e-9, 0.5402985074626867
500e-9, 0.5492537313432837
509.85915492957747e-9, 0.5761194029850747
521.1267605633802e-9, 0.5940298507462688
539.4366197183099e-9, 0.5940298507462688
550.7042253521126e-9, 0.6000000000000001
561.9718309859154e-9, 0.5940298507462688
590.1408450704225e-9, 0.5910447761194031
601.4084507042253e-9, 0.555223880597015
611.2676056338028e-9, 0.5582089552238807
629.5774647887324e-9, 0.5164179104477613
640.8450704225352e-9, 0.5164179104477613
650.7042253521126e-9, 0.4746268656716419
669.0140845070423e-9, 0.43880597014925393
680.2816901408451e-9, 0.4358208955223881
690.1408450704225e-9, 0.40298507462686584
700e-9, 0.42089552238805983
708.450704225352e-9, 0.4119402985074627
721.1267605633802e-9, 0.4238805970149254
729.5774647887324e-9, 0.37910447761194044
739.4366197183099e-9, 0.3880597014925373
749.2957746478874e-9, 0.35820895522388063
760.5633802816901e-9, 0.34626865671641793

Zodiacal Light

```
{"ecliptic_lat": [0.0, 0.17453292519943295, 0.3490658503988659, 0.5235987755982988, 0.6981317007977318, 0.8726646259971648, 1.0471975511965976, 1.2217304763960306, 1.3962634015954636], "ecliptic_lon": [3.141592653589793, 2.792526803190927, 2.443460952792061, 2.0943951023931953, 1.7453292519943295, 1.3962634015954636, 1.1344640137963142, 1.0471975511965976, 0.9599310885968813, 0.8726646259971648, 0.7853981633974483, 0.6981317007977318, 0.6108652381980153, 0.5235987755982988, 0.4363323129985824, 0.3490658503988659, 0.2617993877991494, 0.17453292519943295, 0.08726646259971647, 0.0], "brightness": [[258.0, 211.0, 206.99999999999997, 239.0, 277.0, 365.0, 535.0, 630.0, 756.0, 939.0, 1190.0, 1490.0, 2010.0000000000002, 2940.0, 4660.0, 7690.000000000001, 15100.0, 36500.0, 176000.0, 163000000.0], [212.0, 194.0, 185.0, 217.0, 247.0000000000003, 312.0, 418.0, 455.0, 512.0, 603.0, 696.0, 825.0, 1150.0, 1550.0, 1820.0, 2140.0, 2760.0, 2720.0, 5630.0, 19900.0], [183.0, 174.0, 168.0, 196.0, 220.0000000000003, 258.0, 330.0, 339.0, 358.0, 403.0, 442.0, 512.0, 635.0, 800.0, 932.0, 1070.0, 1120.0, 1390.0, 1700.0, 2290.0], [159.0, 153.0, 152.0, 177.0, 196.0, 219.0, 258.0, 270.0, 282.0, 290.0, 304.0, 331.0, 363.0, 417.0, 491.0, 542.0, 592.0, 655.0, 724.0, 794.0], [141.0, 137.0, 137.0, 161.0, 175.0, 190.0, 204.0, 212.0, 229.0, 227.0, 233.0, 240.0, 224.0000000000003, 241.0, 246.0, 252.0, 265.0, 290.0, 315.0, 403.0], [127.0, 127.0, 128.0, 146.0, 156.0, 166.0, 165.0, 166.0, 183.0, 185.0, 189.0, 186.0, 171.0, 180.0, 183.0, 186.0, 190.0, 199.0, 209.0, 252.0], [117.0, 120.0, 120.0, 132.0, 139.0, 146.0, 137.0, 137.0, 147.0, 149.0, 150.0, 149.0, 137.0, 141.0, 144.0, 145.0, 145.0, 145.0, 146.0, 150.0], [110.0000000000001, 112.0000000000001, 112.0000000000001, 120.0, 123.0, 127.0, 118.0, 120.0, 124.0, 124.0, 124.0, 126.0, 118.0, 120.0, 121.0, 121.0, 121.0, 121.0, 121.0], [103.0, 105.0, 105.0, 108.0, 111.0000000000001, 111.0000000000001, 106.0, 107.0, 107.0, 108.0, 107.0, 111.0000000000001, 107.0, 106.0, 108.0, 108.0, 108.0, 108.0, 108.0]]}
```

Parameter	Value
FWHM	1.5
Sensor dimensions	$0.03690 \times 0.03690 [m]$
<i>f</i> number	7.2
Aperture diameter	$0.35560 [m]$
Secondary diameter	$0.1724660 [m]$
Sensor pixels	4096×4096
Pixel size	$9.009 \cdot 10^{-6} [m/\text{pix}]$
Pixel scale	$0.72545 [\text{arcsec}]$
Field of view	$0.824425^\circ \times 0.824425^\circ$
Integration time	1 [s]

Table 7.1. Purdue Optical Ground Station telescope parameters

7.1.2 Telescope Parameters

Purdue Optical Ground Station

7.1.3 File Formats

Wavefront OBJ Example

```
# Blender v2.92.0 OBJ File: ''
# www.blender.org
mtllib cube.mtl
o Cube_Cube.003
v 1.000000 1.000000 -1.000000
v 1.000000 1.000000 1.000000
v 1.000000 -1.000000 -1.000000
v 1.000000 -1.000000 1.000000
v -1.000000 1.000000 -1.000000
v -1.000000 1.000000 1.000000
v -1.000000 -1.000000 -1.000000
v -1.000000 -1.000000 1.000000
vt 0.625000 0.000000
vt 0.375000 0.250000
vt 0.375000 0.000000
vt 0.625000 0.250000
vt 0.375000 0.500000
vt 0.625000 0.500000
vt 0.375000 0.750000
vt 0.625000 0.750000
vt 0.375000 1.000000
vt 0.125000 0.750000
vt 0.125000 0.500000
vt 0.875000 0.500000
vt 0.625000 1.000000
vt 0.875000 0.750000
vn 1.0000 0.0000 0.0000
vn 0.0000 -1.0000 0.0000
vn -1.0000 0.0000 0.0000
vn 0.0000 1.0000 0.0000
vn 0.0000 0.0000 -1.0000
vn 0.0000 0.0000 1.0000
usemtl None
s off
f 2/1/1 3/2/1 1/3/1
f 4/4/2 7/5/2 3/2/2
f 8/6/3 5/7/3 7/5/3
f 6/8/4 1/9/4 5/7/4
f 7/5/5 1/10/5 3/11/5
f 4/12/6 6/8/6 8/6/6
f 2/1/1 4/4/1 3/2/1
f 4/4/2 8/6/2 7/5/2
f 8/6/3 6/8/3 5/7/3
f 6/8/4 2/13/4 1/9/4
f 7/5/5 5/7/5 1/10/5
f 4/12/6 2/14/6 6/8/6
```

REFERENCES

- [1] ESA Space Debris Office, “Esa’s annual space environment report,” European Space Agency, Tech. Rep., Apr. 2022.
- [2] N. G. S. F. Center, *Vanguard 1*, <https://nssdc.gsfc.nasa.gov/nmc/spacecraft/display.action?id=1958-002B>, Accessed: 2023-09-04.
- [3] D. Vallado, *Fundamentals of Astrodynamics and Applications*, 4th ed. J. Wertz, Ed. Microcosm Press, Mar. 2013.
- [4] C. Frueh, *Space traffic management*, Lecture Notes, 2019.
- [5] S. Fan, “The light curve simulation and its inversion problem for human-made space objects,” Ph.D. dissertation, Purdue University, Aug. 2020. DOI: [10.25394/PGS.12749570.v1](https://doi.org/10.25394/PGS.12749570.v1).
- [6] T. Schildknecht, R. Musci, and M. Fruh C. Ploner, “Color Photometry and Light Curve Observations of Space Debris in GEO,” in *Advanced Maui Optical and Space Surveillance Technologies Conference*, C. Paxson, H. Snell, J. Griffin, *et al.*, Eds., Jan. 2008, E51, E51.
- [7] T. Schildknecht, N. Koshkin, E. Korobeinikova, *et al.*, “Photometric Monitoring of Non-resolved Space Debris and Databases of Optical Light Curves,” in *Advanced Maui Optical and Space Surveillance Technologies Conference*, Jan. 2015, 25, p. 25.
- [8] A. Burton and S. Fan, “Mapping the solution space for light curve attitude estimation,” *43rd COSPAR Scientific Assembly. Held 28 January-4 February*, vol. 43, p. 2193, 2021.
- [9] H. Krag, “A method for the validation of space debris models and for the analysis and planning of radar and optical surveys,” Ph.D. dissertation, Technische Universität Braunschweig, Mar. 2003.
- [10] H. N. Russell, “On the light-variations of asteroids and satellites,” *The Astrophysical Journal*, vol. 24, no. 1, pp. 1–18, 1906.

- [11] M. Kaasalainen and J. Torppa, “Optimization methods for asteroid lightcurve inversion: I. shape determination,” *Icarus*, vol. 153, no. 1, pp. 24–36, 2001, ISSN: 0019-1035. DOI: <https://doi.org/10.1006/icar.2001.6673>. [Online]. Available: <https://www.sciencedirect.com/science/article/pii/S0019103501966734>.
- [12] M. Kaasalainen, J. Torppa, and K. Muinonen, “Optimization methods for asteroid lightcurve inversion: II. the complete inverse problem,” *Icarus*, vol. 153, no. 1, pp. 37–51, 2001, ISSN: 0019-1035. DOI: <https://doi.org/10.1006/icar.2001.6674>. [Online]. Available: <https://www.sciencedirect.com/science/article/pii/S0019103501966746>.
- [13] H. Minkowski, “Allgemeine lehrsätze über die konvexen polyeder,” in *Ausgewählte Arbeiten zur Zahlentheorie und zur Geometrie: Mit D. Hilberts Gedächtnisrede auf H. Minkowski, Göttingen 1909*. Springer Vienna, 1909, ch. 22, pp. 121–139. [Online]. Available: https://doi.org/10.1007/978-3-7091-9536-9_5.
- [14] J. J. Little, “An iterative method for reconstructing convex polyhedra from extended gaussian images,” in *Proceedings of the Third AAAI Conference on Artificial Intelligence*, ser. AAAI’83, Washington, D.C.: AAAI Press, 1983, pp. 247–250.
- [15] J. urech and M. Kaasalainen, “Photometric signatures of highly nonconvex and binary asteroids,” *Astronomy & Astrophysics*, vol. 404, no. 2, pp. 709–714, Jun. 2003. DOI: [10.1051/0004-6361:20030505](https://doi.org/10.1051/0004-6361:20030505).
- [16] C.-K. Chng, M. Sasdelli, and T.-J. Chin, “Globally optimal shape and spin pole determination with light-curve inversion,” *Monthly Notices of the Royal Astronomical Society*, vol. 513, no. 1, pp. 311–332, Jan. 2022, ISSN: 0035-8711. DOI: [10.1093/mnras/stac198](https://doi.org/10.1093/mnras/stac198). eprint: <https://academic.oup.com/mnras/article-pdf/513/1/311/43446894/stac198.pdf>. [Online]. Available: <https://doi.org/10.1093/mnras/stac198>.
- [17] J. Durech, V. Sidorin, and M. Kaasalainen, “DAMIT: a database of asteroid models,” *Astronomy and Astrophysics*, vol. 513, A46, A46, Apr. 2010. DOI: [10.1051/0004-6361/200912693](https://doi.org/10.1051/0004-6361/200912693).
- [18] M. Kaasalainen, J. urech, and V. Sidorin, *DAMIT: Database of Asteroid Models from Inversion Techniques*, Astrophysics Source Code Library, record ascl:1412.004, Dec. 2014. ascl: [1412.004](https://doi.org/10.1781/ascl.1412.004).
- [19] B. Calef, J. Africano, B. Birge, D. Hall, and P. Kervin, “Photometric signature inversion,” in *Unconventional Imaging II*, V. L. Gamiz, P. S. Idell, and M. S. Strojnik, Eds., International Society for Optics and Photonics, vol. 6307, SPIE, 2006, pp. 141–150. DOI: [10.1117/12.683015](https://doi.org/10.1117/12.683015). [Online]. Available: <https://doi.org/10.1117/12.683015>.

- [20] B. K. Bradley and P. Axelrad, “Lightcurve inversion for shape estimation of geo objects from space-based sensors,” in *Proceedings of the International Symposium on Space Flight Dynamics*, 2014, pp. 1–20.
- [21] S. Fan and C. Frueh, “A direct light curve inversion scheme in the presence of measurement noise,” *The Journal of the Astronautical Sciences*, vol. 67, Aug. 2019. DOI: [10.1007/s40295-019-00190-3](https://doi.org/10.1007/s40295-019-00190-3).
- [22] S. Fan and C. Frueh, “Multi-hypothesis light curve inversion scheme for convex objects with minimal observations,” in *Proceedings of the 8th European Conference on Space Debris*, ESA Space Debris Office, 2021, pp. 1–7.
- [23] A. M. Friedman, “Observability analysis for space situational awareness,” Ph.D. dissertation, Purdue University, Apr. 2020. DOI: [10.25394/PGS.12196863.v1](https://doi.org/10.25394/PGS.12196863.v1).
- [24] A. M. Friedman and C. Frueh, “Observability of light curve inversion for shape and feature determination exemplified by a case analysis,” *Journal of the Astronautical Sciences*, vol. 69, no. 2, pp. 537–569, Apr. 2022. DOI: [10.1007/s40295-021-00293-w](https://doi.org/10.1007/s40295-021-00293-w).
- [25] D. V. Cabrera, J. Utzmann, and R. Förstner, “Inversion of the shape of space debris from non-resolved optical measurements within spook,” in *Proceedings of the 22nd Advanced Maui Optical and Space Surveillance Technologies Conference*, 2021, pp. 1–18.
- [26] R. Linares, M. Jah, and J. Crassidis, “Inactive space object shape estimation via astrometric and photometric data fusion,” *Advances in the Astronautical Sciences*, vol. 143, pp. 217–232, Jan. 2012.
- [27] R. Linares, M. K. Jah, J. L. Crassidis, and C. K. Nebelecky, “Space object shape characterization and tracking using light curve and angles data,” *Journal of Guidance, Control, and Dynamics*, vol. 37, no. 1, pp. 13–25, 2014. DOI: [10.2514/1.62986](https://doi.org/10.2514/1.62986).
- [28] R. Linares and J. L. Crassidis, “Space-object shape inversion via adaptive hamiltonian markov chain monte carlo,” *Journal of Guidance, Control, and Dynamics*, vol. 41, no. 1, pp. 47–58, 2018.
- [29] R. Linares and R. Furfaro, “Space object classification using deep convolutional neural networks,” in *19th International Conference on Information Fusion*, Jul. 2016, pp. 1–8.

- [30] E. Kerr, G. P. Elisabeth, P. Talon, and D. Petit, “Using ai to analyse light curves for geo object characterisation,” in *Proceedings of the 22nd Advanced Maui Optical and Space Surveillance Technologies Conference*, 2021, pp. 1–9.
- [31] K. McNally, D. Ramirez, A. M. Anton, D. Smith, and J. Dick, “Artificial intelligence for space resident objects characterisation with lightcurves,” in *Proceedings of the 8th European Conference on Space Debris*, ESA Space Debris Office, 2021, pp. 1–12.
- [32] J. Allworth, L. Windrim, J. Bennett, and M. Bryson, “A transfer learning approach to space debris classification using observational light curve data,” *Acta Astronautica*, vol. 181, pp. 301–315, Jan. 2021. DOI: [10.1016/j.actaastro.2021.01.048](https://doi.org/10.1016/j.actaastro.2021.01.048).
- [33] S. Karpov, E. Katkova, G. Beskin, *et al.*, “Massive photometry of low-altitude artificial satellites on Mini-Mega-TORTORA,” in *Revista Mexicana de Astronomia y Astrofisica Conference Series*, ser. Revista Mexicana de Astronomia y Astrofisica Conference Series, vol. 48, Dec. 2016, pp. 112–113.
- [34] C. Benson, D. Scheeres, and N. Moskovitz, “Light curves of retired geosynchronous satellites,” in *7th European Conference on Space Debris*, vol. 7, 2017, p. 04.
- [35] N. Koshkin, L. Shakun, E. Korobeynikova, *et al.*, “Monitoring of space debris rotation based on photometry,” *Odessa Astronomical Publications*, vol. 31, pp. 179–185, 2018.
- [36] Y. Wang, X. Du, J. Zhao, Z. Yin, and Y. Song, “What causes the abrupt changes in the light curve of a geo satellite?” *Acta Astronautica*, vol. 153, pp. 130–137, 2018, ISSN: 0094-5765. DOI: <https://doi.org/10.1016/j.actaastro.2018.10.035>. [Online]. Available: <https://www.sciencedirect.com/science/article/pii/S0094576518313857>.
- [37] S. Fan, C. Frueh, and A. Buzzoni, “A light curve simulation of the apollo lunar ascent module,” in *AIAA/AAS Astrodynamics Specialist Conference*, 2016, pp. 1–10. DOI: [10.2514/6.2016-5504](https://doi.org/10.2514/6.2016-5504).
- [38] D. Kobayashi and C. Frueh, “Compressed sensing for satellite characterization,” in *Proceedings of the 20th AAS/AIAA Astrodynamics Specialist Conference*, Aug. 2020, pp. 1–20.
- [39] C. Früh and M. K. Jah, “Coupled orbit attitude motion of high area-to-mass ratio (hamr) objects including efficient self-shadowing,” *Acta Astronautica*, vol. 95, pp. 227–241, 2014, ISSN: 0094-5765. DOI: <https://doi.org/10.1016/j.actaastro.2013.11.017>.

- [40] J. Allworth, L. Windrim, J. Wardman, D. Kucharski, J. Bennett, and M. Bryson, “Development of a high fidelity simulator for generalised photometric based space object classification using machine learning,” in *Proceedings of 70th International Astronautical Congress*, International Astronautical Congress, 2019, pp. 1–14. DOI: [10.48550/ARXIV.2004.12270](https://doi.org/10.48550/ARXIV.2004.12270). [Online]. Available: <https://arxiv.org/abs/2004.12270>.
- [41] R. Furfaro, R. Linares, and V. Reddy, “Shape Identification of Space Objects via Light Curve Inversion Using Deep Learning Models,” in *Proceedings of the 20th Advanced Maui Optical and Space Surveillance Technologies Conference*, S. Ryan, Ed., Sep. 2019, 17, p. 17.
- [42] L. D. J. Blacketer, “Attitude characterisation of space objects using optical light curves,” Ph.D. dissertation, University of Southampton, Mar. 2022. [Online]. Available: <https://eprints.soton.ac.uk/457200/>.
- [43] F. L. Markley and J. L. Crassidis, *Fundamentals of Spacecraft Attitude Determination and Control*. Springer, May 2014.
- [44] M. D. Shuster, “Survey of attitude representations,” *Journal of the Astronautical Sciences*, vol. 41, no. 4, pp. 439–517, Oct. 1993.
- [45] D. Newell and E. Tiesinga, *The international system of units (si), 2019 edition*, en, Aug. 2019. DOI: <https://doi.org/10.6028/NIST.SP.330-2019>.
- [46] L. T. Sharpe, A. Stockman, W. Jagla, and H. Jägle, “A luminous efficiency function, $V^*(\lambda)$, for daylight adaptation,” *Journal of Vision*, vol. 5, no. 11, pp. 3–3, Dec. 2005, ISSN: 1534-7362. DOI: [10.1167/5.11.3](https://doi.org/10.1167/5.11.3). eprint: https://arvojournals.org/arvo/content/_public/journal/jov/932833/jov-5-11-3.pdf. [Online]. Available: <https://doi.org/10.1167/5.11.3>.
- [47] K. A. Pickering, “The Southern Limits of the Ancient Star Catalog and the Commentary of Hipparchos,” *DIO*, vol. 12, pp. 3–27, Sep. 2002.
- [48] F. Falchi, P. Cinzano, D. Duriscoe, *et al.*, *Supplement to: The new world atlas of artificial night sky brightness. v. 1.1. gfz data services*. <https://doi.org/10.5880/GFZ.1.4.2016.001>, Accessed: 2023-08-25, 2016.
- [49] F. Falchi, P. Cinzano, D. Duriscoe, *et al.*, “The new world atlas of artificial night sky brightness,” *Science Advances*, vol. 2, no. 6, e1600377, 2016. DOI: [10.1126/sciadv.1600377](https://doi.org/10.1126/sciadv.1600377). eprint: <https://www.science.org/doi/pdf/10.1126/sciadv.1600377>. [Online]. Available: <https://www.science.org/doi/abs/10.1126/sciadv.1600377>.

- [50] F. Patat, O. S. Ugolnikov, and O. V. Postylyakov, “UBVRI twilight sky brightness at ESO-Paranal,” *Astronomy and Astrophysics*, vol. 455, no. 1, pp. 385–393, Aug. 2006. DOI: [10.1051/0004-6361:20064992](https://doi.org/10.1051/0004-6361:20064992). arXiv: [astro-ph/0604128 \[astro-ph\]](https://arxiv.org/abs/astro-ph/0604128).
- [51] A. e. a. Vallenari, “Gaia Data Release 3. Summary of the content and survey properties,” *Astronomy & Astrophysics*, vol. 674, A1, A1, Jun. 2023. DOI: [10.1051/0004-6361/202243940](https://doi.org/10.1051/0004-6361/202243940). arXiv: [2208.00211 \[astro-ph.GA\]](https://arxiv.org/abs/2208.00211).
- [52] J. C. Segovia, *Astroquery.gaia package*, <https://astroquery.readthedocs.io/en/latest/gaia/gaia.html>, Accessed: 2023-08-21, 2016.
- [53] G. M. Daniels, “A night sky model for satellite search systems.,” *Optical Engineering*, vol. 16, pp. 66–71, Feb. 1977.
- [54] F. E. Roach, “A Photometric Model of the Zodiacal Light,” *Astronomical Journal*, vol. 77, p. 887, Dec. 1972. DOI: [10.1086/111363](https://doi.org/10.1086/111363).
- [55] *Wavefront obj file format*, <https://www.loc.gov/preservation/digital/formats/fdd/fdd000507.shtml>, Accessed: 2023-08-30, 2020.
- [56] B. Duvenhage, K. Bouatouch, and D. Kourie, “Numerical verification of bidirectional reflectance distribution functions for physical plausibility,” in *SAICSIT ’13: Proceedings of the South African Institute for Computer Scientists and Information Technologists Conference*, Oct. 2013, pp. 200–208, ISBN: 9781450321129. DOI: [10.1145/2513456.2513499](https://doi.org/10.1145/2513456.2513499).
- [57] R. M. Soldado and C. U. Almagro, “An overview of brdf models,” 2012. [Online]. Available: <https://api.semanticscholar.org/CorpusID:44900609>.
- [58] B. T. Phong, “Illumination for computer generated pictures,” in *Seminal Graphics: Pioneering Efforts That Shaped the Field*. New York, NY, USA: Association for Computing Machinery, 1998, pp. 95–101, ISBN: 158113052X. [Online]. Available: [%5Curl%7Bhttps://doi.org/10.1145/280811.280980%7D](https://doi.org/10.1145/280811.280980).
- [59] R. L. Cook and K. E. Torrance, “A reflectance model for computer graphics,” *ACM Trans. Graph.*, vol. 1, no. 1, pp. 7–24, Jan. 1982, ISSN: 0730-0301. DOI: [10.1145/357290.357293](https://doi.org/10.1145/357290.357293). [Online]. Available: <https://doi.org/10.1145/357290.357293>.

- [60] M. Oren and S. K. Nayar, “Generalization of lambert’s reflectance model,” in *Proceedings of the 21st Annual Conference on Computer Graphics and Interactive Techniques*, ser. SIGGRAPH ’94, New York, NY, USA: Association for Computing Machinery, 1994, pp. 239–246, ISBN: 0897916670. DOI: [10.1145/192161.192213](https://doi.org/10.1145/192161.192213). [Online]. Available: <https://doi.org/10.1145/192161.192213>.
- [61] M. Ashikhmin and P. Shirley, “An anisotropic phong brdf model,” *Journal of Graphics Tools*, vol. 5, Jan. 2001. DOI: [10.1080/10867651.2000.10487522](https://doi.org/10.1080/10867651.2000.10487522).
- [62] T. Möller and B. Trumbore, “Fast, minimum storage ray-triangle intersection,” *Journal of Graphics Tools*, vol. 2, Aug. 2005. DOI: [10.1145/1198555.1198746](https://doi.org/10.1145/1198555.1198746).
- [63] W. Keeter, *Nasa 3d models*, <https://nasa3d.arc.nasa.gov/models/>, Accessed: 2022-04-27, Feb. 2013.
- [64] H. Kolivand and M. S. Sunar, “Survey of shadow volume algorithms in computer graphics,” *IETE Technical Review*, vol. 30, no. 1, pp. 38–46, 2013. DOI: [10.4103/0256-4602.107338](https://doi.org/10.4103/0256-4602.107338).
- [65] S. Brabec, T. Annen, and H.-P. Seidel, “Practical shadow mapping,” *Journal of Graphics Tools*, vol. 7, no. 4, pp. 9–18, 2002.
- [66] R. Santamaría, *Raylib*, <https://www.raylib.com>, Accessed: 2022-04-28, Nov. 2021.
- [67] J. J. Little, “Extended gaussian images, mixed volumes, shape reconstruction,” in *Proceedings of the First Annual Symposium on Computational Geometry*, ser. SCG ’85, Baltimore, Maryland, USA: Association for Computing Machinery, 1985, pp. 15–23, ISBN: 0897911636. DOI: [10.1145/323233.323236](https://doi.org/10.1145/323233.323236). [Online]. Available: <https://doi.org/10.1145/323233.323236>.
- [68] C. L. Lawson and R. J. Hanson, “Solving least squares problems,” in *Classics in applied mathematics*, 1976. [Online]. Available: <https://api.semanticscholar.org/CorpusID:122862057>.
- [69] R. Bro and S. De Jong, “A fast non-negativity-constrained least squares algorithm,” *Journal of Chemometrics*, vol. 11, no. 5, pp. 393–401, 1997. DOI: [https://doi.org/10.1002/\(SICI\)1099-128X\(199709/10\)11:5<393::AID-CEM483>3.0.CO;2-L](https://doi.org/10.1002/(SICI)1099-128X(199709/10)11:5<393::AID-CEM483>3.0.CO;2-L). [Online]. Available: <https://onlinelibrary.wiley.com/doi/abs/10.1002/%28SICI%291099-128X%28199709/10%2911%3A5%3C393%3A%3AAID-CEM483%3E3.0.CO%3B2-L>.

- [70] B. Keinert, M. Innmann, M. Sänger, and M. Stamminger, “Spherical fibonacci mapping,” *ACM Transactions on Graphics*, vol. 34, no. 6, pp. 1–7, 2015.
- [71] E. W. Weisstein, *Sphere point picking*, <https://mathworld.wolfram.com/SpherePointPicking.html>, Accessed: 2022-07-03, 2002.
- [72] C. T. Loop, “Smooth subdivision surfaces based on triangles,” Ph.D. dissertation, University of Utah, Aug. 1987. [Online]. Available: <https://www.microsoft.com/en-us/research/publication/smooth-subdivision-surfaces-based-on-triangles/>.
- [73] A. Bærentzen and H. Aanæs, “Generating signed distance fields from triangle meshes,” Jan. 2002.
- [74] W. E. Lorensen and H. E. Cline, “Marching cubes: A high resolution 3d surface construction algorithm,” in *Proceedings of the 14th Annual Conference on Computer Graphics and Interactive Techniques*, ser. SIGGRAPH ’87, New York, NY, USA: Association for Computing Machinery, 1987, pp. 163–169, ISBN: 0897912276. DOI: [10.1145/37401.37422](https://doi.org/10.1145/37401.37422). [Online]. Available: <https://doi.org/10.1145/37401.37422>.
- [75] W. Schroeder, R. Maynard, and B. Geveci, “Flying edges: A high-performance scalable isocontouring algorithm,” Oct. 2015. DOI: [10.13140/RG.2.1.3415.9609](https://doi.org/10.13140/RG.2.1.3415.9609).